Sea ice in the Arctic Transpolar Drift in 2020/21: thermodynamic evolution of different ice types

Ruibo Lei[1*], Mario Hoppmann[2], Bin Cheng[3], Marcel Nicolaus[2], Fanyi Zhang[1,4], Benjamin Rabe[2], Long Lin[1], Julia Regnery[2], Donald K. Perovich[5]

[1] Key Laboratory for Polar Science of the MNR, Polar Research Institute of China, Shanghai, China;

[2] Alfred Wegener Institute, Helmholtz Centre for Polar and Marine Research, Bremerhaven, Germany;

[3] Finnish Meteorological Institute, Helsinki, Finland;

[4] Chinese Antarctic Center of Surveying and Mapping, Wuhan University, Wuhan, China;

[5] Thayer School of Engineering, Dartmouth College, Hanover, NH, USA;

Correspondence to: Ruibo Lei (leiruibo@pric.org.cn)

Abstract. Sea ice properties are extremely inhomogeneous, in particular on the floe-scale. Different characteristic local features, such as melt ponds and pressure ridges, profoundly impact the thermodynamic evolution of the ice pack even in a kilometre-scale domain, and the associated processes are still not well represented in current climate models. To better characterize the freezing and melting of different types of sea ice, we deployed four sea ice mass balance buoys on an ice floe close to the North Pole during the second drift of the Multidisciplinary drifting Observatory for the Study of Arctic Climate (MOSAiC) in August 2020. The study sites included level first-year ice, an open melt pond, and an unconsolidated ridge. The floe slowly drifted southwards from October 2020 to early March 2021 but shifted to a more rapid drift from March to July 2021. This drifting pattern, together with a large snow accumulation, relatively warm air temperatures, and a rapid increase in oceanic heat close to Fram Strait, determined the seasonal evolution of the ice mass balance. Storms, accompanied by higher air temperatures and enhanced ice dynamics, were the main cause of the formation of snow ice or superimposed ice. Although the 0.24-m deep melt pond was completely refrozen by 5 September, the relatively large snow accumulation and the heat storage with the rotten ice layer delayed ice basal growth beyond the last observation at this site in mid-February 2021. At the ridge site, the macroporosity of the unconsolidated layer was estimated between 0.005 and 0.755. The freezing of internal voids also delayed the ridge basal growth, which was not observed until 26 April 2021. Thus, the refreezing of ponded ice and voids within the unconsolidated ridges amplifies the anisotropy of the heat exchange between the ice and the lower atmosphere/upper ocean. Our results provide an important physical background for further interdisciplinary studies related to the MOSAiC observations and can be used to optimize the parameterization of freezing processes related to melt ponds and ice ridges in sea ice numerical models.

1 Introduction

Arctic sea ice restricts the direct exchanges of mass, energy, and momentum between the atmosphere and ocean. Since the geometric scale of Arctic sea ice thickness versus its area/range is extreme (m vs. 10^8 km^2), sea ice thermodynamic growth and decay processes are particularly susceptible to the changes of atmospheric and oceanic forcing. In recent decades, the icescape of Arctic Ocean that was formerly dominated by multi-year ice has gradually shifted to first-year ice (Stroeve and Notz, 2018). The amplification of Arctic climate warming, the increased absorption of solar radiation by the ice-ocean system in summer, as well as the changes in the physical natures of the sea ice itself, favor the advanced onset of sea ice melt and the delayed occurring of ice freezing at both the ice surface and bottom (Lin et al., 2022). The extended duration of the melt season also leads to an increase in melt pond area on the ice (Lee et al., 2020). The formation and refreezing of the melt ponds are in particular expected to highly amplify the seasonal evolution of the ice albedo (Perovich et al., 2002), and consequently the heat budget of the entire ice-ocean system (Nicolaus et al., 2012). Thus, melt pond processes contribute to the regulation of the interannual changes in summer Arctic sea ice extent to a significant degree (Schroder et al., 2014). Further, the thinning of Arctic sea ice also promotes the formation of saline melt ponds. Compared to fresh ponds, the stronger salt stratification of a saline pond can enhance the heat flux down into the ice, causing additional ice melt (Kim et al., 2018).

The reductions of Arctic sea ice thickness and concentration result in an enhanced response of ice motion to wind forcing (Rampal et al., 2009; Zhang et al., 2021), and thus in an increased mobility and deformation rate of the ice pack (Lei et al., 2020). Thereby, the production of first-year pressure ridges through the collision or shearing of floes is also enhanced (Weeks, 2010; Strub-Klein and Sudom, 2012). During this process, a pronounced sail (keel) component above (below) water level is formed through compressing and piling up the disordered ice rubbles. In Fram Strait, which is one of the main export gateways of Arctic sea ice, the deformed ice constituted on average 66% of the total ice thickness from 1990 to 2011 (Hansen et al., 2014). Thus, the ice ridges are expected to represent a significant portion of the sea ice volume in the entire Arctic Ocean (Farrell et al., 2020). Within the newly-formed ice ridges, voids filled with seawater are present between randomly distributed ice rubble, constituting an unconsolidated ice layer (Strub-Klein and Sudom, 2012). Different from the ice microporosity defined by brine and air volume fractions (Cox and Weeks, 1983), the proportion of these voids are defined as macroporosity (Leppäranta et al., 1995). The voids between the ice rubble immersed in the seawater can freeze in winter (Leppäranta et al., 1995; Høyland, 2002; Ervik et al., 2018; Shestov et al., 2018), which generates heat through a phase transition. The freezing unconsolidated ridge layers (and melt pond) also alters the local hydrostatic balance, and consequently the elevation of the ice surface, which in turn impacts the ice thickness retrieved by satellite altimetry (e.g., Farrell et al., 2020; Landy et al., 2022). In addition, since the strength of the consolidated layer is markedly different from that of an unconsolidated layer, their geometric dimensions are the crucial parameters to define the overall mechanical

60 strength of an ice ridge (Chai et al., 2020). Through replenishing nutrients from the upper ocean, a higher photosynthetic

61 radiation flux because of being closer to the ice surface (Lu et al., 2018) or guiding through ridge cavities (Katlein et al.,

62 2021), and protection against marine mesozooplankton grazing under the ice, melt ponds and cavities within unconsolidated

63 ridges may constitute a small-scale ecosystem and promote algal growth (e.g., Fernández-Méndez et al., 2018; Hancke et al.,

64 2022). Thus, cross-season observations of melt pond and unconsolidated ice ridges, especially during the melt-freezing

65 transition, can help to improve the implementation of associated processes in sea ice numerical models and to evaluate their

66 impacts on sea ice mass balance and the ice-associated ecosystem on various scales. However, such observations are

67 extremely rare in the central Arctic Ocean. Especially for the consolidation process of first-year ice ridges, most observations

68 have been performed in the Arctic peripheral seas (e.g., Høyland and Løset, 1999; Høyland, 2002) or subarctic regions (e.g.,

69 Leppäranta et al., 1995), and are only available for a relatively short time (e.g., Ervik et al., 2018; Shestov et al., 2018).

70   The Multidisciplinary drifting Observatory for the Study of Arctic Climate (MOSAiC) expedition provided a unique

71 opportunity to observe cross-sphere interactions in the central Arctic Ocean over an entire annual cycle (Nicolaus et al., 2022;

72 Rabe et al., 2022; Shupe et al., 2022). During the first drift of MOSAiC from October 2019 to July 2020, i.e. Legs 1–4, a

73 variety of methods were applied to observe sea ice mass balance at the Central Observatory (CO) and the surrounding

74 Distributed Network (DN) on a scale of up to 50 km (Nicolaus et al., 2022). This included for example various types of sea

75 ice mass balance buoys (IMBs; Lei et al., 2022), airborne electromagnetic induction sounding (von Albedyll et al., 2022),

76 ground-based transect surveys using GEM-2 and Magnaprobe instruments, and Remotely Operated Vehicle (ROV)-borne

77 multibeam sounding (Katlein et al., 2020). However, the observations made during this first MOSAiC drift missed the initial

78 freezing process, which usually occurs in late August to September for the ice surface (Persson, 2012). Based on

79 observations collected by the MOSAiC DN, Lei et al. (2022) characterized in detail the freezing processes of level ice with

80 various initial thicknesses. However, this study did not include the freezing process of ponded and ridged ice. After its first

81 drift, the MOSAiC expedition returned to the pack ice zone close to the geographic North Pole (Figure 1) and installed a new

82 camp, referred to as CO3 (short for Central Observatory 3), to complete the entire annual cycle. The CO3 drift began on 21

83 August and ended on 21 September 2020. Observations were focused on processes related to the melt-freezing transition

84 (Nicolaus et al., 2022). The CO3 ice floe was predominantly composed of first-year ice, but with a complex icescape of

85 about 30% open melt ponds (Webster et al., 2022) and 30% deformed ice, which provided an opportunity to quantify the

86 freezing process of sea ice with a variety of different initial conditions. Analyses of transect surveys of snow and melt ponds

87 (Webster et al., 2022), and albedo (Light et al., 2022) already revealed that the surfaces of the snow/scatting layer, melt

88 ponds, and leads have entered the freezing season before the ship left the CO3 floe on 21 September 2020. After the ship

89 departed from the CO3 floe, the basal ice growth, melt-pond refreezing, and consolidation of ice ridges were subsequently

90 observed by four snow and ice mass balance arrays (SIMBAs) that were deployed on representative sampling sites with

91   different sea ice characteristics.

92   In this study, we use these four buoy time series, combined with auxiliary in-situ measurements, atmospheric reanalysis,

93   and satellite remote sensing data to describe in detail the freezing process of three different sea ice types from late summer to

94   winter 2020. Moreover, we characterize the thawing processes during the spring-summer transition in 2021, when the buoys

95   approached Fram Strait and the Greenland Sea (Figure 1). Finally, we also compare our results to SIMBA data obtained from

96   deployments in previous years that exhibited a similar drift trajectory starting from the same season, to determine the

97   interannual differences in the seasonal evolution of the sea ice mass balance.

98
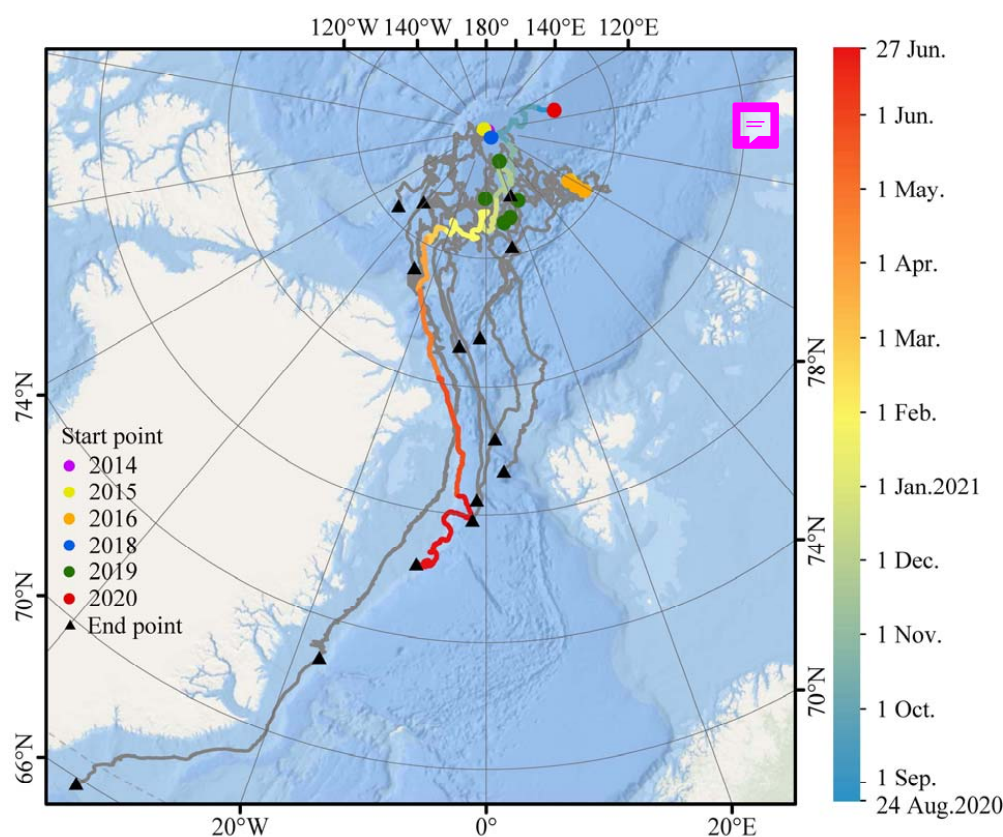
99   **Figure 1.** Drift trajectories of the SIMBA-type sea ice mass balance buoys described in this paper. The colored trajectories represent the
100   buoys deployed at the MOSAiC Leg 5 ice floe (CO3) in late summer 2020, which are the focus of this study; the gray lines represent the
101   buoys deployed in other years, that are used here for comparison; the solid colored dots are the locations of the initial buoy deployment in
102   the various years; the black triangles are the positions where the buoys ceased their operation.

103   **2 Data and methods**

2.1 Ice conditions and deployment sites

In July 2020, the first MOSAiC ice floe finally broke apart in Fram Strait (CO1 and CO2; Nicolaus et al., 2022), which concluded the first MOSAiC drift. In early August 2020, *Polarstern* relocated to a new ice floe at 87.70°N and 104.50°E, to begin a second drift in order to complete the full annual cycle. ~~The expedition is referred to as MOSAiC Leg 5.~~ On 21 August 2020, a new ice camp, referred to as CO3, was established on the floe. Initially, the CO3 floe had a diameter of ~500 m and a melt-pond coverage of ~30% (Figure 2). Towards the site where R/V *Polarstern* was ~~anchoring,~~ the icescape was characterized by a massive and highly deformed ice ridge (30% in total areal coverage), and the areal coverage of melt ponds was relatively low; the other 70% of the floe was dominated by either level ice or ponded ice. Initial surveys showed that the average ice thickness was about 1.5 m, with a modal thickness of about 1.2 m (representing level ice). The thickness of the ice ridges was between 3.0 and 8.0 m. The ice was covered by either coarse-grained snow or a scattering layer, both between 0.04 and 0.10 m ~~depth,~~ which were generally difficult to distinguish (Light et al., 2022). Approximately half of the melt ponds were still open, while the other half had a ~ 0.01-m layer of ~~thin~~ ice ~~on top~~. The melt ponds ~~had water~~ depths ~~of~~ ~0.20–0.40 m (Webster et al., 2022).

~~During MOSAiC Leg 5,~~ five thermistor-chain-style IMBs (four SIMBA-type and one Bruncin-type) were deployed on the CO3 floe to measure sea ice temperature and heating profiles during the campaign and beyond. Since the Bruncin-type IMB only collected data until late October 2020, we here only use data from the four SIMBAs for further analysis. These SIMBA-type IMBs (designed and manufactured by the Enterprise of Scottish Association for Marine Science Research, Scotland) are equipped with a 5.12 m long thermistor chain integrating 256 thermistors at 0.02 m spacing (Jackson et al., 2013). The environment temperatures (ET) of each thermistor along the chain were recorded simultaneously at a 6-hour interval, and the temperature change around the sensors after a weak pulse of heating (HT) was recorded daily after heating cycles of 30 s and 120 s, respectively. An additional thermistor was used to measure the near-surface air temperature at about ~1 m height.

The four SIMBAs were deployed at study sites representing three different ice types. Two buoys (IDs 2020T78 and 2020T84) were installed on level ice with initial ice thicknesses of 1.48 and 1.12 m, respectively. We also refer to these two sites/units as "Level 1" and "Level 2" (for level ice), respectively. SIMBA 2020T81 was installed in an open melt pond with an initial pond depth and ice thickness underneath of 0.24 and 0.96 m, respectively. We refer to this site/unit as "Pond". Finally, SIMBA 2020T85 was installed on a small ridge with an initial ice thickness of 4.00 m. We refer to this site/unit as "Ridge". See Table 1 for an overview. During the installation of the thermistor chain in the ridge crest using a 55-mm diameter auger, voids were occasionally noticed for the lower portion. The ridge was only partially consolidated, with a sail height of 0.75 m, and a keel depth of 3.25 m. This included a top consolidated portion of 1.90 m and a lower unconsolidated

134   portion of 1.35 m. Based on a comprehensive analysis of the morphology of first-year ice ridges using history data over the

135   entire Arctic, Strub-Klein, and Sudom (2012) determined the averages of the ice thickness, sail, keel, and consolidated layer

136   as 4.90, 0.80, 4.80, and 1.77 m, respectively. Thus, although the observed ridge was relatively small, it still can be considered

137   representative with respect to its geometric dimensions and proportion of the consolidated layer.

138   The SIMBA was also equipped with a tilt sensor (FXOS8700CQ, NXP Semiconductors, Netherlands). Thus, the roll,

139   pitch, and plane rotation of the instrument deployed on the ice surface (Figure 2) can be obtained by analyzing the

140   acceleration relative to the orthogonal triaxis. These attitude parameters were used to identify fracturing events, ice melt

141   beneath the instrument, or movement caused by polar bears. At the pond site, the SIMBA was co-deployed with a radiation

142   buoy (ID 2020R21), which was used to measure surface albedo and under-ice light transmission using three spectral

143   radiometers (Ramses, TriOS GmbH, Germany). In this study, we used the data to quantify the impact of the initial freezing

144   process of the melt pond on the change in surface albedo. In the center of the CO3 floe, a CTD chain buoy (ID 2020O10,

145   Pacific Gyre, California, US), consisting of 5 SBE37IMP microcats operated on an inductive modem tether, was deployed on

146   28 August 2020 to measure the seawater temperature, conductivity (salinity) and pressure at five depths (Hopmman et al.,

147   2022). We used the measurements of the CTD at the shallowest depth of 10 m to characterize the changes in the oceanic

148   mixed layer and its coupling with the ice basal growth.

149   After the initial buoy deployments, the CO3 floe drifted northeastwards and reached its northernmost point at 89.60°N

150   and 110.42°E by 26 September 2020. Subsequently, the floe drifted to 86.31°N, 26.43°W (11 February 2021) and 86.15°N,

151   26.90°W (26 February 2021), where data transmission of the Pond and Level 1 buoys suddenly stopped. The Level 2 and

152   Ridge buoys continued to drift southwards following the Arctic Transpolar Drift (TPD) and ceased their temperature

153   measurements close to the ice edge at 78.50°N, 3.26°W (2 June 2021), and 76.33°N, 9.00°W (27 June 2021), respectively.

154   **Table 1.** Deployment information of the SIMBAs on the CO3 floe

Name /Buoy ID	Deployment date (yyyy-mm-dd)	Measurement ending date (yyyy-mm-dd)	Measurement ending location	Initial ice thickness /m	Initial snow or scatting layer depth /m	Initial pond depth /m
Level 1 2020T78	2020-08-23	2021-2-26	86.15°N, 26.90°W	1.48	0.08	N/A
Level 2 2020T84	2020-08-26	2021-06-02	78.50°N, 3.26°W	1.12	0.06	N/A
Pond 2020T81	2020-08-30	2021-02-11	86.31°N, 26.43°W	0.96	N/A	0.24
Ridge 2020T85	2020-09-19	2021-06-27	76.33°N, 9.00°W	4.00	0.06	N/A

155
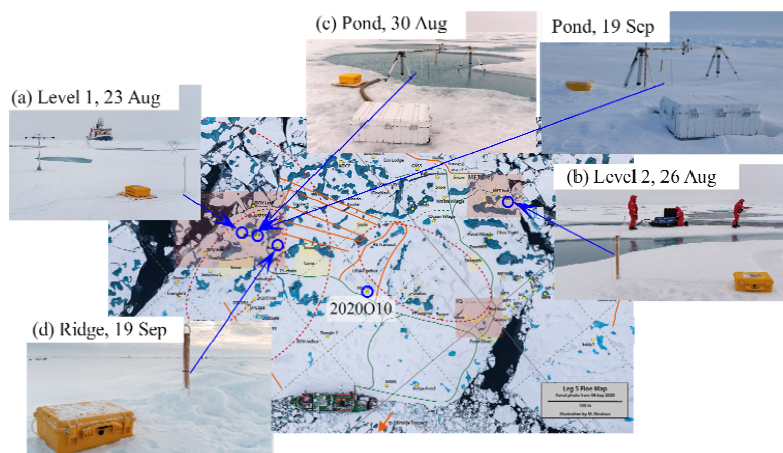
Figure 2. Annotated aerial image of the MOSAiC CO3 floe obtained on 6 September 2020, along with photos of the different SIMBAs analyzed in this study. R/V *Polarstern* is anchored to the floe at the bottom of the image, the orange lines denote specific observation areas/transects, the small yellow dots denote different instrument deployment sites, and the blue circles highlight the four SIMBA and the CTD buoy sites. Photos of the four buoys right after the deployment are shown in the additional panels: (a) Level 1 deployed on 23 August at the main buoy site; (b) Level 2 deployed on 26 August at Met City; (c) Pond deployed on 30 August in an open melt pond with a radiation buoy 2020R21, and also shown is this site with the snow-covered refrozen pond on 19 September; and (d) Ridge deployed on 19 September over a small ridge. The aerial image was compiled by Steffen Graupner from a large number of individual drone images, which were took by himself.

2.2 Analysis of thermistor chain profile data

The SIMBA temperature (ET) and heated temperature (HT) profiles were used to determine the interfaces between air, snow, snow ice or superimposed ice (if exists), sea ice, and seawater. This is possible based on the different responses of these mediums to a heating pulse due to their differing thermodynamic properties (Jackson et al., 2013). Note that, at the ridge site, the macroporosity of the unconsolidated layer restricted the establishment of a vertical temperature gradient. Thus, the blue line shown in Figure 3d was the breaking point between the upper near-linear temperature gradient and the lower isothermal line, which can be defined as the interface between the consolidated and unconsolidated ice layers.

To compare the sea ice mass balance from our study sites to that obtained in previous years, we co-analyzed several datasets from SIMBAs deployed in 2014–2019. Constraining the measurements to a similar region and timeframe, we only selected data from buoys deployed in or drifting into the region north of 87°N from mid-August to later September. These prerequisites were met by a total of 11 additional SIMBAs deployed during various R/V *Polarstern* Arctic expeditions, and the TICE expedition by the *Akademik Tryoshnikov* (Figure 1).
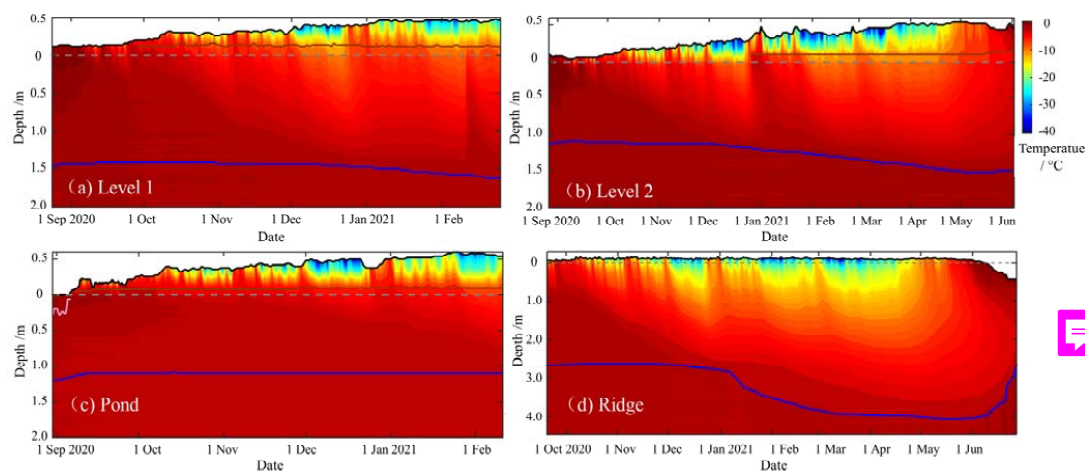
Figure 3. Seasonal evolution of the snow-ice-water temperature profiles measured by the four SIMBAs. Also shown are the snow surface (black line), the interface between snow and snow ice (brown line), the initial interface between snow and sea ice (dashed grey line, also used as the zero reference), as well as (a–c) the ice bottom or (d) lower boundary of consolidated ice layer (blue line).

2.3 Calculations of the heat flux

The conductive heat flux (F_c) produced by the vertical temperature gradient and the specific heat (F_s) caused by the temporal change in temperature through the ice cover together determine how the sea ice reaches a thermodynamic balance with the atmosphere and ocean. Thus, we compared the thermodynamic processes of sea ice with different initial conditions by quantifying the conductive and specific heat fluxes through the ice. To evaluate the role of oceanic heat flux on sea ice growth, we calculated the oceanic heat flux (F_w) based on the heat balance at the ice bottom (McPhee and Untersteiner, 1982). We calculated the latent heat flux (F_l) according to the ice growth rate, and the conductive and specific heat fluxes through a 0.30-m thick reference layer at a distance of 0.20 m from the ice bottom. The residual then represents the oceanic heat flux. To estimate F_c and F_s, we assume a sea ice salinity of 1.0 for the top 0.40 m of ice to represent typical conditions after desalination, a salinity of 2.5 for the lower ice layer after representative in-situ ice-core measurements at the CO3 floe, and a typical salinity of 6.0 for newly-formed ice. In addition, to estimate F_l, we assume a sea ice salinity of 8.0 and an ice density of 910 kg m^{-3} at the ice bottom. The freezing point was time-dependent and here approximated using measurements by the CTD buoy at a depth level of 10 m. To estimate F_w, we used the 15-d averaged heat fluxes to reduce the uncertainties of measurements and parameterizations.

At the ridge site, before the lower boundary of the consolidated ice layer reached the keel bottom, we can only obtain the freezing rate of the consolidated layer based on the temperature profile. Thus, the F_w estimated using the residual energy method was not possible before this point in time. However, during this stage, we can estimate the macroporosity (r) of the unconsolidated ice layer at its upper boundary based on the heat balance (Leppäranta et al., 1995):

198

199    $F_c + F_l + F_s - F_w = 0$,   (1)

200   and $F_l = - r\rho_{si}L_f\frac{\partial Z_{si}}{\partial t}$,   (2)

201   where ρ_{si}, L_f, and $\partial Z_{si}/\partial t$ are sea ice density, the latent heat of fusion, and the ice growth rate, respectively. The sign

202   convention is such that upward, melting, and warming heat fluxes are positive; otherwise, they are negative. Note that the

203   ocean heat flux used to estimate the macroporosity of the unconsolidated ice layer was obtained from the estimation at the

204   Level 2 site by assuming a consistent ocean heat flux beneath the two sites with a distance of 300 m. Although the roughness

205   of the ice bottom would in principle affect the heat exchange between the ocean and the ice (Wettlaufer, 1991), such a

206   mechanism generally produces pronounced effects on a short-term scale. The difference between the two sites can thereby be

207   neglected for the 15-d average. Another assumption is that no heat was consumed or generated due to the melting or freezing

208   of the unconsolidated ice layer, except for that occurring at its upper boundary. The estimation of the ice ridge macroporosity

209   started from the point in time when the freezing front reached the bottom of the consolidated layer (in mid-November 2020),

210   until when the front reached the ice keel bottom (by mid-April 2021). During this period, the ocean mixed layer was at a

211   temperature close to the freezing point (see Figure S1 in Supplementary material). Thereby, it is assumed that the ice rubble

212   at the top of the ocean mixed layer neither froze nor melted. To test the sensitivity of the results with regard to this

213   assumption, we also presumed that 50% of the oceanic heat flux was consumed to melt the ice rubble initially and that this

214   consumption decreased linearly with the distance from the bottom of the consolidated layer. In this sensitivity calculation,

215   the oceanic heat flux was given as:

216    $F_{wt} = 0.5 \, F_w \, (d_t/d_0+1)$,   (3)

217   where F_w and F_{wt} are the oceanic heat flux estimated from the Level 2 site and that assumed for the sensitivity

218   calculation at time t, respectively; d_t and d_0 are the distance from the bottom of the consolidated layer to the keel bottom at

219   the time t and that (1.35 m) at the initial stage (26 November). Although this sensitivity test has some arbitrariness, it still can

220   qualitatively assess the uncertainty of the estimated macroporosity caused by ignoring the consumption of the oceanic heat

221   flux in the unconsolidated layer. In addition, we note that the macroporosity of the unconsolidated ice layer estimated here

222   corresponds to the value at a given depth at the time of calculation. As time goes on, the cavities between the ice rubbles can

223   undergo changes caused by buoyancy, mechanical erosion due to ocean currents, or bending failure of ice blocks (Leppäranta

224   et al., 1995; Ervik et al., 2018).

225 **2.4 Analysis of other parameters related to ice mass balance**

226   Incident and reflected spectral radiation in the band from 350 to 920 nm measured by the radiation buoy over the pond

227 was used to analyze the influence of the melt pond refreezing process on the evolution of the surface albedo.

228   We calculated the Central Arctic air pressure gradient Index (CAI), defined as the difference in sea level air pressure

229 (SLP) between 90°W and 90°E at 84°N, which indicates the intensity of the TPD (Vihma et al., 2012) to identify anomalies

230 in atmospheric circulation patterns during the study year and their influences on the seasonal evolution of sea ice mass

231 balance. Atmospheric reanalysis data of near-surface air temperature (2 m, T_{2m}), wind speed (10 m, W_{10m}), surface net

232 short-wave and long-wave radiations, turbulent fluxes of sensible and latent heat, obtained from the ERA-5 dataset of the

233 European Centre for Medium-Range Weather Forecasts (ECMWF). T_{2m} was used to calculate the accumulated Freezing

234 Degree Days (FDD), which is commonly considered the best meteorological measure of sea ice thermodynamic growth (e.g.,

235 Leppäranta, 1993). We then calculated the sum of the four ERA-5 surface radiation and turbulence fluxes, referred as the net

236 surface-atmosphere heat flux, to evaluate the contribution of atmospheric forcing to the heat balance at the ice surface, with a

237 positive value indicating upward heat flux.

238   Daily sea ice concentration (Fetterer et al., 2017) and motion speed (Tschudi et al., 2020) retrieved from the Nimbus-7

239 Scanning Multichannel Microwave Radiometer and its successors (1979–2021), as well as weekly merged CryoSat-2–SMOS

240 sea ice thickness (2010–2021) retrieved from the CryoSat-2 altimeter and the SMOS radiometer (Ricker et al., 2017) were

241 used to estimate anomalies of ice conditions along the buoy's trajectory during the study period.

242   Bathymetric data along the buoys' trajectory was obtained from the Version 3.0 data of the International Bathymetric

243 Chart of the Arctic Ocean (Jakobsson et al., 2012).

244 **3 Results**

245 **3.1 General atmospheric and sea ice conditions during the ice season**

246   In September 2020, the CAI was slightly larger than the 1979–2020 climatology (see Figure S2 in Supplementary

247 material). From October 2020 to February 2021, the CAI gradually decreased below the climatology. From April to June

248 2021, the CAI increased markedly and remained above the climatology by more than one standard deviation. Accordingly,

249 the drift trajectory of the CO3 floe was quite tortuous and was dominated by zonal advection from October 2020 to February

250 2021. Afterward, the floe drifted rapidly to the south (Figure 1).

251   Between late August and early September 2020, T_{2m} stayed above or close to 0°C (Figure 4a). The ERA-5 net

252   surface-atmosphere heat flux maintained negative (Figure 4f), suggesting that the atmospheric conditions had not yet

253   transitioned to a stage conducive to freezing. Subsequently, T_{2m} gradually decreased and reached a winter typical

254   low-temperature stage from mid-December 2020 to late March 2021. At the same time, the floe also experienced several

255   low-pressure synoptic events during the freezing season, especially from mid-November to late December 2020 and in late

256   February 2021, which were accompanied by pronounced increases in T_{2m}. On 12 November and 25 December 2020, T_{2m} rose

257   to –0.9 °C and –3.6 °C, respectively. Since early April 2021, T_{2m} gradually increased again and reached 0 °C by 30 May 2021.

258   From then onward, T_{2m} stayed close to or above 0°C. Compared to the 1979–2020 climatology, the frequent low-pressure

259   systems combined with the Arctic amplification resulted in a T_{2m} higher than the climatology from September to March. In

260   April–May 2021, the floe experienced relatively cold weather. As a result, the accumulated FDDs were lower than the

261   1979–2020 climatology from 17 September 2020 onward. The net surface-atmosphere heat flux was generally positive

262   (upward), but smaller than the climatology. However, this heat flux shifted to downward during episodic warming events,

263   suggesting that the ice layer gained heat from the atmosphere. From mid-May 2021 onward, this heat flux gradually

264   decreased and stayed negative, indicating that atmospheric conditions transitioned to a stage conducive to ice melt. On

265   average, T_{2m} was higher than the climatology by 1.9 °C and the magnitude of the net surface-atmosphere heat flux was lower

266   than the climatology by 10.9 W m^{-2} from September 2020 to June 2021. This indicates that the atmospheric conditions in the

267   study year were generally not conducive to the sea ice growth.

268   The wind forcing during the study period was comparable to the 1979–2020 climatology (Figure 4c). However, the ice

269   drift speed was much larger than the 1979–2020 climatology (Figure 4d), which is likely related to the enhanced response of

270   the sea ice to wind stress as the pack ice becomes increasingly younger and thinner (e.g., Zhang et al., 2021). Due to the

271   dominance of low-pressure systems during most of November–December 2020, the precipitation rate in this period was

272   much larger compared to the 1979–2020 climatology (Figure 4e), which resulted in an accumulated precipitation larger than

273   the climatology by one standard deviation for November 2020 to mid-May 2021. The ice concentration remained close to

274   100% until mid-May 2021 (Figure 4g). Afterward, the ice concentration declined drastically to 50% by 27 June 2021 at

275   76.3°N. The CryoSat-2–SMOS data reveals that the ice was relatively thin in mid-October 2020 compared to the 2011–2020

276   average (Figure 4h). The temporal variations in sea ice thickness obtained by satellite altimetry generally exhibited a greater

277   fluctuation compared to the buoy observations because the former includes the contribution of dynamic thickening (e.g., Koo

278   et al., 2021). The CryoSat-2–SMOS ice thickness increased from 1.60 m in mid-October 2020 to 2.62 m by mid-April 2021,

279   In the same period, the ice thickness derived from SIMBA measurements at the Level 2 site only increased from 1.16 to 1.48

280   m. The difference was likely related to that 1) the relatively larger snow depth at the Level 2 site could reduce the ice growth,

281   and 2) the ice dynamics resulted in the ice thickness redistribution, which cannot be captured by the buoy measurements. In

282   addition, the abnormally large precipitation equivalent in the study region during the year 2020–2021 (Figure 4b), which

283   may lead to a larger accumulation of snow, as well as formations of snow ice or superimposed ice, in the observation

284   footprint of Ku-band synthetic aperture radar altimeter of CryoSat-2. Both processes can lead to the reduction of the

285   penetrability of the altimeter in the snow layer (Ricker et al., 2014; Stroeve et al., 2022), thus leading to larger ice freeboard

286   and greater retrieved ice thickness. This effect would be amplified during the freezing season as the snow thickening, which

287   may also lead to a greater sea ice growth rate obtained by the CryoSat-2–SMOS product compared to the buoy measurement.

288
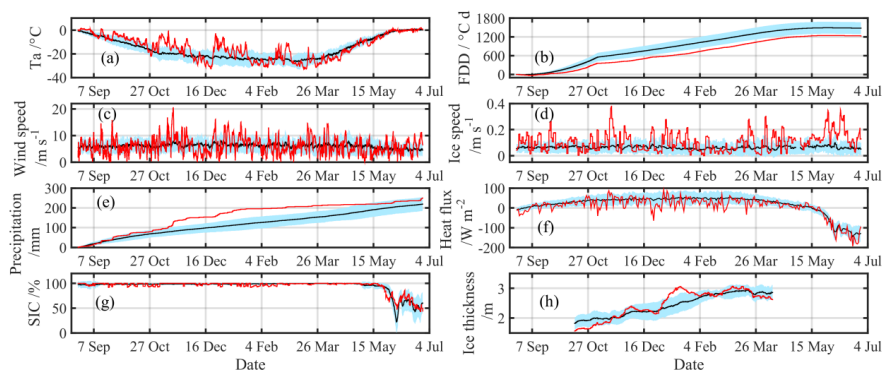
289   **Figure 4.** Time series of (a) near-surface (2 m) air temperature, (b) accumulated freezing degree days (FDD), (c) near-surface (10 m) wind

290   speed, (d) ice drift speed, (e) accumulated precipitation, (f) ERA-5 net surface-atmosphere heat flux, (g) ice concentration, and (h) ice

291   thickness. The red lines denote data from 2020–2021, and the black line with cyan shadow denotes the multi-year average and standard

292   deviation (2011–2020 for ice thickness, and 1979–2020 for others).

293   **3.2 Onset of sea ice freezing**

294   Initial surveys on 21 August 2020 yielded pond fractions of 35–48% and pond depths of about 0.25–0.35 m over an area

295   of 100 m by 200 m and a 1.5-km transect (Webster et al., 2022). By 6 September, all melt ponds on the survey transects were

296   frozen. Thus, both the initial depth and the refreezing observed at the Pond site can be considered representative of CO3. As

297   shown in Figure 5a, the near-surface air temperature measured by the SIMBA (T_{buoy}) declined gradually from 1 to 2°C on

298   26–30 August to –7 to –4°C by 9 September, and the seawater temperature just under the ice layer also dropped by about

299   0.03°C during this period. By 3 September, the 14-d running average T_{buoy} fell below –0.1 °C, which indicates the ice surface

300   freezing onset (Persson, 2012). With the decrease in T_{buoy}, the melt pond surface gradually refroze. The aerial images (Figure

301   5c–5f) revealed that the obvious change on the pond surface occurred between 6 and 7 September, with the color changing

302   from emerald green to gray. As snow is subsequently deposited on the newly-formed ice, the color of the pond changes to

303   grayish white by 11 September, and it becomes more difficult to distinguish the pond from the surrounding snow-covered

304   level ice. The 350–920 nm integrated albedo on the open pond was around 0.32 from 28 to 30 August. This broadband

305   albedo remained <0.50 from 30 August to 4 September and exhibited some fluctuations associated with repeated

306   freezing-thawing and sporadic snow deposition. Subsequently, the broadband albedo increased markedly and ranged between

307   0.65–0.85 by 7–9 September, which was close to the albedo of the non-ponded snow-covered ice. Thus, the refrozen pond

308   and the accumulated snow on the surface could be considered optically thick by that time. The albedo evolution of our Pond

309   site was similar to other ponds along the "Kinder Albedo line", a dedicated 140–200 m transect over the CO3 floe (Light et

310   al., 2022), which also revealed a distinct increase on September 5 due to the freezing.

311   The Pond temperature profile time series was also used to characterize in more detail the internal refreezing process of

312   the melt pond. From 30 August to 3 September, the water temperatures within the melt pond (depth 0.24 m) were between

313   –0.4 and –0.1 °C and there was no distinct vertical temperature gradient (Figure 5b). This indicates that the melt pond was

314   still open and well mixed. However, by 5 September, a reverse temperature gradient started to establish within the pond,

315   which was continuous with the temperature gradient of the ice layer underneath. By that time, the temperature gradient

316   through the entire ice column was nearly the same as that of level ice. Therefore, the refreezing process through the full

317   depth of the melt pond must have been completed by then. Subsequently, snow began to accumulate on the surface of the

318   refrozen pond. Because the surface of the refrozen pond was slightly lower than the surrounding level ice, snow tended to

319   accumulate there. This process may significantly reduce the radiation flux through the pond, making the pond changing from

320   bright window to dark spot rapidly (e.g., Anhaus et al., 2021). By 9 September 2020, the snow depth over the refrozen pond

321   increased to 0.22 m. In contrast to the surface refreezing, the ice bottom at this site had melted by 0.06 m during this stage,

322   which was larger than at the other three sites. This was likely due to the ice layer under the pond being mostly rotten and

323   therefore permeable, which allowed the warm seawater to intrude upwards and promote ice basal melt.

324
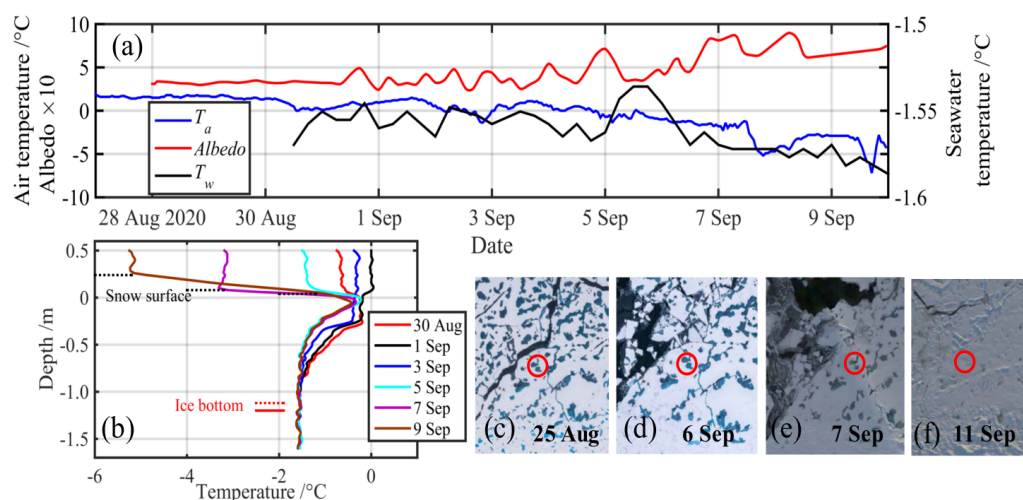
325   **Figure 5.** Time series of near-surface air temperature and vertically averaged seawater temperature under the ice (3–4 m from the ice

326   surface) measured by the SIMBA, and 350–920 nm integrated albedo measured by the radiation buoy; (b) six selected temperature profiles

327   from 30 August to 9 September. Also shown are the snow surface on 5, 7, and 9 September (black dashed lines), as well as the ice bottom

328   on 30 August (red line) and 9 September (red dashed line); (c–f) aerial RGB images (provided by Steffen Graupner), with the red circles

329   denoting the Pond site.

330   In the following, we use the data measured at the Level 1 site to characterize the transition from melting to freezing for

331 a representative level ice column. The temperature at the interface between snow and ice decreased below 0°C on 2

332 September (Figure 6a). Subsequently, the ice started to cool from both above and below (Figure 6b). However, a pronounced

333 warm air intrusion event occurred on 13–14 September, which was also accompanied by rainfall (Gabarró et al., 2022;

334 Stroeve et al., 2022). This rain-on-snow event resulted in a slight snow melt of ~ 0.04 m, and a temporary warming of the top

335 ice layer. The liquid water deposited on the existing snowpack during this event has produced icy crusts at the surface or

336 within the snowpack upon refreezing, resulting in the formation of superimposed ice at some sites of the CO3 (Stroeve et al.,

337 2022). However, no superimposed ice was observed at the Level 1 site. It was likely because the formation of superimposed

338 ice also depends on the permeability of the ice layer underneath (e.g., Provost et al., 2019). At this site, the relatively warm

339 ice layer during that time suggests a comparably high ice porosity and permeability. In contrast, superimposed ice of about

340 0.08 m was observed on the refrozen Pond site since 14 September (Figure 3c). This can be attributed to two potential

341 mechanisms: 1) the newly-frozen ice layer on the pond surface was close to the freshwater ice, thus its permeability was

342 expected to be much lower compared to the top layer of the residual level ice, and 2) both the relatively thick snow and the

343 slightly recessed surface of the refrozen pond have the potential to provide more meltwater to produce superimposed ice.

344   From 15 September 2020 onward, the ice at the Level 1 site has entered the cooling stage, with the freezing front

345 gradually expanding downward. However, another episodic warming event occurred on 24–26 September, with near-surface

346 air temperature increasing to –0.4°C, which resulted in snow melt and warming of the top ice layer again. Different from the

347 early warming event on 13–14 September, this process subsequently produced a superimposed ice layer of about 0.12 m on

348 top of the original ice layer on 25 September 2020. It was because the colder ice layer on the top likely had a decreased

349 permeability, which favored the formation of superimposed ice. The accumulation of fresh snow after the formation of the

350 superimposed ice resulted in a rapid increase in snow depth. From mid-October onward, the atmospheric cooling led to the

351 ice layer entering a rapid cooling stage. Finally, initial ice basal growth started on 31 October 2020, and relatively stable ice

352 growth was observed from 13 December 2020 onward. Therefore, compared to the atmospheric and oceanic forcing entering

353 the freezing season in mid-September (Rinke et al., 2021; Kawaguchi et al., 2022), the ice bottom began to grow ~2 months

354 later for the level ice (1.42 m), which could be mainly attributed to the release of specific heat from the thermal storage of

355 ice layer itself (e.g., Lin et al., 2022). From mid-September to mid-December 2020, the accumulation of snow from 0.14 to

356 0.42 m was significantly greater than that observed on the level ice over the MOSAiC CO1 floe, where snow depth increased

357 to ~0.15 m only by mid-December 2019 (Lei et al., 2022; Wagner et al., 2022). This discrepancy can be related to the

358 relatively large cumulative precipitation equivalent (138 mm) from 15 September to 31 December 2020, which was ~75%

359 larger than the 1979–2020 Climatology (Figure 4e).

360   The evolution of ice cooling and freezing onset was generally similar at the Level 1 and Level 2 sites. However, at the

361   refrozen Pond site, the onset of basal ice growth was still not observed by the end of the buoy lifetime on 11 February

362   (Figure 3). Three potential factors could have delayed sea ice cooling and basal ice growth at this site: 1) the latent heat

363   caused by refreezing of the melt pond, 2) the latent heat produced by the refreezing of larger brine channels and pockets in

364   the rotten ice below the pond, and 3) the large snow deposition due to the recessed pond surface. Similarly, at the Ridge site

365   there was a large portion of unconsolidated ice in the lower layer, and the ice basal growth at that site has not been observed

366   until the freezing front reached the keel bottom by mid-April 2021.

367
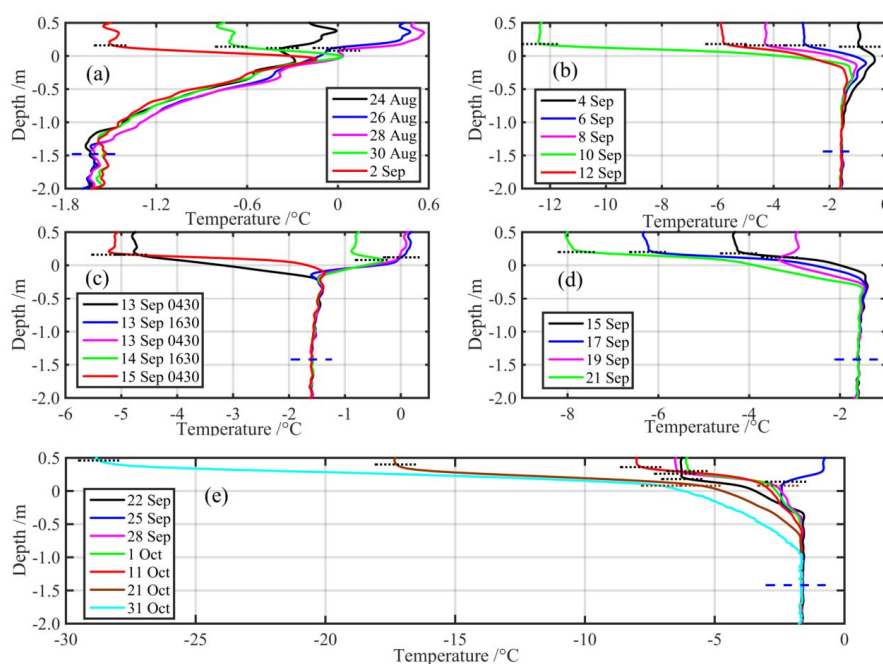
Figure 6. Selected vertical temperature profiles of air-snow-ice-seawater at the Level 1 site: (a) 24 August to 2 September 2020, melting

stage; (b) 4 to 12 September 2020, surface starting to freeze; (c) 13 to 15 September 2020, with a rain-on-snow event occurring on 13–14

September; (d) 15 to 21 September 2020, top layer reentering the cooling period and the ship departing from the CO3 floe on 20

September; and (e) 22 September to 31 October 2020, freezing front gradually extending downward and initial ice basal growth occurring

on 31 October, with an episodic warming event occurring on 25 September.

3.3 Total ice growth and melt season

374   Only two of the buoys remained operational until the beginning of the melt season. At the Level 2 site, the snow

375   temperatures gradually increased from April 2021 onward, as spring came and the floe drifted further to the south. The melt

376   onsets at the snow surface and the ice bottom occurred almost simultaneously when the floe drifted towards Fram Strait at

377   about 80.9°N by 17 May 2021. The total ice growth at this site was 0.50 m, with 0.14 m occurring at the top surface and 0.36

378   m at the ice bottom. The basal ice growth was half of that (0.72 m) observed at the L2 site of MOSAiC DN by 17 May 2020

379 (Lei et al., 2022), where the initial ice thickness was close to that at Level 2 site (1.16 m at Level 2 vs. 1.10 m at L2 on 1

380 November). This difference can attributed to the relatively larger snow depth (0.39 m) and smaller FDD (4390 °C·d)

381 obtained at the Level 2 site of CO3 during the period from 1 November to 17 May than those (0.19 m and 4638 °C·d) for the

382 L2 site of DN. The difference in FDD corresponds an air-temperature deviation of 1.3 °C. The date of ice basal melt onset at

383 the Level 2 site of CO3 was about one month earlier (in the respective years) than that observed at the L2 site of MOSAiC

384 DN. This was because the L2 floe drifted to the marginal ice zone (MIZ) in Fram Strait later in the year, by 19 July 2020 (Lei

385 et al., 2022), which suggests that the time of reaching the MIZ has a large influence on regulating the seasonality of sea ice

386 mass balance in the TPD. Further comparisons with similar measurements from other years in the TPD region will be

387 presented in the next section. At the time of surface melt onset at the Level 2 site, a newly-formed, 0.02–0.04 m thick layer

388 of superimposed ice caused by the refreezing of percolating meltwater was observed on top of the original snow ice layer.

389 The maximum ice thickness of 4.08 m was observed at the Ridge site on 13 May 2021. The total basal ice growth at that

390 site was 0.08 m, which was only 22% of the basal ice growth at the Level 2 site, although the timing of the ice basal melt

391 onset was close at both sites. Thus, the mass budget of the ice ridge was dominated by the consolidation process of the

392 initially unconsolidated layer. Finally, associated with the larger ice thickness, the Ridge site survived for a longer period

393 while drifting close to the ice edge. The buoy ceased to report temperature data by 27 June 2021 at 76.3°N and 9.0°W. By

394 that time, the ice basal melt had reached 1.40 m, which was about three times the melt observed at the surface (0.42 m). This

395 was expected due to the rapid increase in oceanic heat flux under the ice close to the ice edge.

396 **3.4 Heat balance at the ice surface**

397 As the snow texture and density change frequently as a result of repeated thawing-freezing and weathering processes,

398 the parameterization of the snow thermal conductivity coefficient poses a great challenge without any in-situ observations

399 from snow pits (Sturm et al., 1997). Therefore, we analyze the heat balance at the ice surface by comparing the conductive

400 heat flux through the surface ice layer (0.15 m) against the ERA-5 net surface-atmosphere heat flux. Although the conductive

401 heat fluxes at the surface ice layer of the four observation sites were significantly correlated with the net surface-atmosphere

402 heat flux, they all had obvious discrepancy, and the discrepancies of each site were greatly inconsistent (Figure 7). Firstly, we

403 can attribute this discrepancy to potential errors in the ERA-5 reanalysis product of heat flux. Secondly, the inconsistency of

404 the discrepancy of each measurement can be attributed to the differences of snow and ice conditions between the measuring

405 sites. In addition, the discontinuity of conductive heat fluxes through the snow and the surface ice layer, caused the phase

406 change and solar heating within the snow cover (Sturm et al., 2002) also would lead to the discrepancy between the

407 conductive heat fluxes obtained from the measurements and the ERA-5 net surface-atmosphere heat flux.

408 The conductive heat flux through the surface ice layer of the ridge was larger than that at other sites, which is explained

409   by its relatively thin snow cover. At this site, the average surface conductive heat flux was 48% larger than the net surface

410   atmospheric heat flux. In contrast to that, at the Pond site, the surface conductive heat flux was 87% smaller than the net

411   surface atmospheric heat flux, which could be related to the large snow accumulation over the refrozen pond. It is worth

412   noting that the surface conductive heat flux at the Pond site was very close to that at the Level 1 site after 5 September, due

413   to a similar snow depth at the two sites. This evidence confirms that, compared to the regular level ice, the delayed cooling

414   of the lower ice layer and basal growth at the Pond site was not caused by the discrepancy of heat flux at the surface, but

415   related to the difference in the internal structure of the original ice layer. In the comparably warm periods at the beginning of

416   the measurements (before 5 September 2020) and the period after mid-May 2021, the heat gained from the atmosphere did

417   not result in an immediate change in surface conductive heat flux. This was because the additional heat at this stage was used

418   to melt the snow or ice at the surface, but not to change the ice temperature.

419   Considering the entire observation period, the surface conductive heat fluxes can be explained by the ERA-5 surface net

420   atmospheric heat flux by 25–31% (P <0.001) at the two Level ice sites (Figure 7b and 7c), by 20% (P <0.01) at the Pond site

421   (Figure 7d), and by 55% (P <0.001) at the Ridge site (Figure 7e). This discrepancy was mainly caused by the difference in

422   snow depth, and secondly dependent on whether the observation period included the melt stages before 5 September 2020 or

423   after mid-May 2021. Note that we obtained the best correlation with the conductive heat flux being delayed by one day

424   relative to the net surface atmospheric heat flux at the Level ice sites, by two days for the Pond site, and without any delay

425   for the Ridge site. Thus, the comparably thick snow at the Level and Pond sites delayed the thermodynamic response of sea

426   ice to atmospheric forcing. During the period from late September 2020 to late February 2021, when all instruments were

427   still operational, the average surface conductive heat flux of the four sites could be explained by the net surface atmospheric

428   heat flux by 37%, with a ratio of 0.61 between them. Although the deployment sites were considered generally representative

429   of the CO3 floe, the small number of sampling sites, the fact that new ice in leads is not represented, the influence of phase

430   transitions within the snow cover, combined with the inherent uncertainty of the reanalyzed atmospheric heat flux, together

431   affect this ratio. Therefore, when we evaluate the heat balance between the atmosphere and sea ice, the heterogeneities of

432   snow and sea ice conditions and their temporal changes cannot be ignored, even at the floe scale.
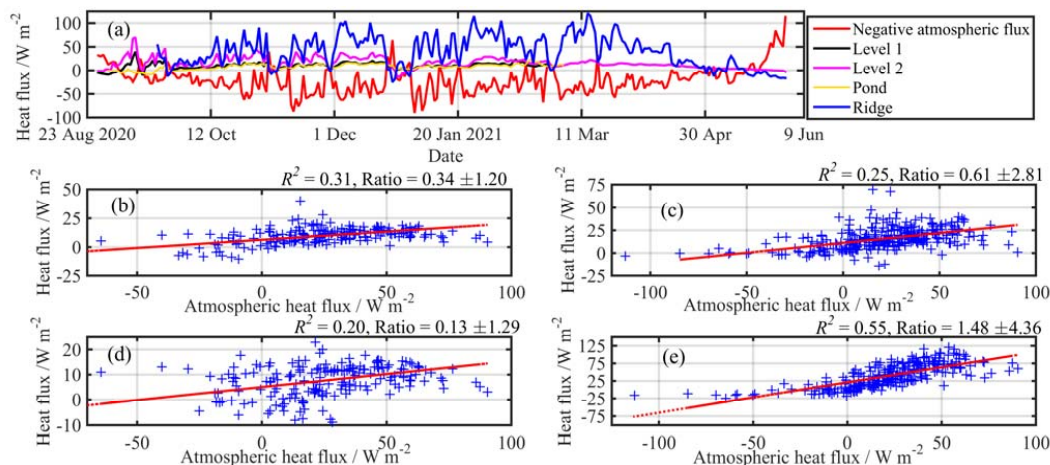
Figure 7. (a) The net surface atmospheric heat flux and conductive heat flux through the surface ice layer; note that the atmospheric heat flux was multiplied by –1 for purposes of readability. The statistical relations between the surface conductive heat flux and the net surface atmospheric heat flux at the (b) Level 1, (c) Level 2, (d) Pond, and (e) Ridge sites. Also shown are the R^2 values and ratios.

3.5 Heat balance at the ice bottom

Similar to previous studies (e.g., Perovich and Elder, 2002; Lei et al., 2022), the basal ice growth at the Level sites was mainly dominated by the oceanic and conductive heat fluxes (Figure 8a and 8b). Since the temperature variability at the basal ice layer was very small, the specific heat flux only showed episodic increases during the dynamic events (will be discussed later). Seasonally, the oceanic heat flux decreased from ~5.0 W m^{-2} in early September to less than 2.8 W m^{-2} by the end of September 2020. This heat flux remained low until mid-April 2021 when the floe drifted to 83.4°N over the northeastern Greenland continental slope. Afterward, the oceanic heat flux increased gradually to 11.0 W m^{-2} by mid-May in the Fram Strait. The seasonal variation in the oceanic heat flux was consistent with the deviation of the seawater temperature under the ice from the freezing point (Figure 8b). This implies that the seasonality of the oceanic heat flux was mainly modulated by the heat content of the oceanic mixed layer. In turn, the increased solar radiation absorbed by the upper ocean and the increased heat supply from the underlying warm Atlantic Water to sea ice (e.g, Duarte et al., 2020) were the main contributions to the increase in the oceanic heat content in and south of the Fram Strait.

It should be noted that the results for the latent heat and oceanic heat fluxes calculated using the Pond (Figure 11c) and Ridge (Figure 11d) site data are mostly unreasonable. At the Pond site, the latent heat flux was generally underestimated as it is only taking into account the heat caused by the basal ice freezing, but neglecting the refreezing of the brine channels within the rotten ice interior. In contrast, the latent heat flux at the Ridge site was overestimated because it was determined using the consolidation rate of the unconsolidated ice layer. Here, we used the oceanic heat flux estimated from the Level 2 site (Figure 8b), and the conductive and specific heat fluxes obtained from the consolidated ice layer (Figure 8d) to estimate

455   the macroporosity of the ridge following Equation 1. As shown in Figure 8f, the macroporosity ranged from 0.005 to 0.755.

456   The macroporosity varied greatly with the depth. This phenomenon has been confirmed by many borehole surveys (e.g.,

457   Høyland, 2002; Shafrova and Høyland, 2008; Kharitonov, 2012; Ervik et al., 2018). Close to the keel bottom, a large

458   macroporosity can generally be expected because of the strength of the erosion caused by the ocean current. At a depth level

459   of ~2.80 m, the high macroporosity suggests that this part was dominated by the presence of large voids, while the low

460   macroporosity at depths from 3.02 to 3.92 m indicates that the ridge was dominated by ice blocks. The average

461   macroporosity at depths of 2.65 to 4.00 m was 0.186, which is close to the average (0.199) obtained from other observations

462   across the Arctic Ocean (Strub-Klein and Sudom, 2012). In addition, if we assume that a part of the oceanic heat flux is

463   consumed to melt the ice rubbles (Eq. 3), the vertical average macroporosity was estimated as 0.222, which is 19% higher

464   compared to that estimated by absolutely neglecting the consumption of oceanic heat flux. Thus, we argue that the

465   calculation of the ridge macroporosity is insensitive to the parameterization of the oceanic heat flux, mainly because it was

466   comparably weak during the freezing season.

467   After the freezing front extended beyond the keel bottom, the estimated latent heat and oceanic heat fluxes at this site

468   can be considered reasonable, as the conditions become similar to the Level site. By 9 June 2021, when the floe had drifted

469   to 77.5°N and 5.1°W, the estimated oceanic heat flux increased to 70 W m^{-2} (Figure 8b), and the resulting ice basal melt

470   rate reached 0.007 m d^{-1} (Figure 8e).

471
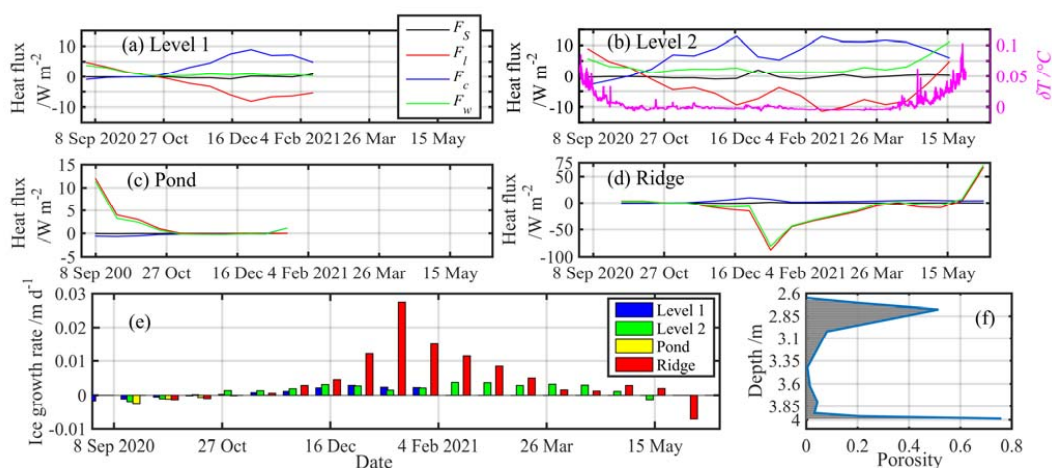
472   **Figure 8.** Time series of specific heat (F_s), equivalent latent heat (F_l), conductive heat (F_c), and oceanic heat fluxes (F_w) calculated at the

473   basal layer of the (a) Level 1, (b) Level 2, and (c) Pond sites, and (d) at the lower boundary of consolidation layer of the Ridge site; (e)

474   15-day average sea ice growth rate or consolidation rate; (f) vertical changes in macroporosity of the ridge unconsolidated layer.

475   **4 Discussion**

4.1 Influence of synoptic events on ice freezing

As shown in Figure 3, both the temporal variation and the vertical gradient of the ice temperatures were greatly affected by the synoptic systems, especially from early November to mid-December 2020, when the synoptic event was relatively frequent and the sea ice has not entered a stable growth period. Thus, we focus on this period to identify the influence of synoptic events on ice freezing. Among the sites, the magnitude of the impact differed strongly (Figure 9). At the Level sites (Figure 9c–9f), the influence of the synoptic processes on the heat fluxes within the ice layer reached as far as ~0.7–1.0 m deep into the ice, depending on the duration and intensity of the respective event. For example, during 4–8 November (3–9 December), the persistent warming (cooling) caused a substantial decrease (increase) in the heat fluxes through the ice. The relatively large snow depth (~0.10 m) and ice thickness (~0.35 m) at the Level 1 site resulted in smaller heat fluxes compared to the Level 2 site by ~50% in the top ice layer. At the Pond site, since the freezing front still hadn't reached the lower ice layer, the influence of air temperature fluctuations was only observed within the top 0-0.40 m of the ice (Figure 9g–9h). This difference again corroborates the influence of the refreezing of pond water and brine channels within the underlying ice on the ice cooling.

At the Ridge site, the snow depth was generally less than 0.16 m, which is much smaller than the snow depth at the other sites. Thus, the heat flux at the top ice layer was also larger (Figure 9i–9j) than at other sites. Compared to level ice, the heat flux through the ice ridge became much smaller from the surface to the ice interior, which was likely related to the larger freeboard (or sail) component (0.76 m at the beginning of measurement) of the ridge compared to the Level sites (less than 0.20 m). The ridge sail presumable had a relatively high porosity due to meltwater percolation during the previous summer and cavities not being completely filled by snow, which would lead to additional insulation for the heat flow (Høyland and Løset, 1999).
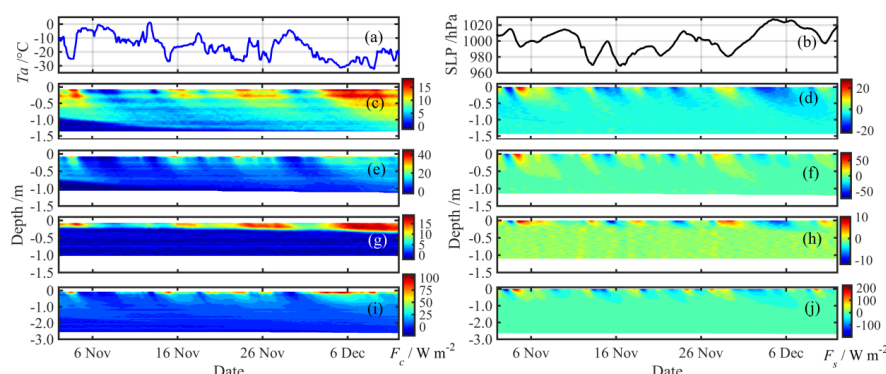
Figure 9. Time series of (a) near-surface air temperature and (b) sea level air pressure (SLP) measured at Level 1 site, and conductive and specific heat fluxes for the period from 2 November to 11 December 2020 at the different sites: (c and d) Level 1, (e and f) Level 2, (g and h) Pond, and (i and j) Ridge.

500   In addition to the intrusions of warm air masses, low-pressure synoptic systems also bring storm events, which bear the

501   potential to cause increased sea ice fracturing. Two such dynamic events were recorded by the built-in attitude sensors

502   (Figure 10). These were accompanied by drastic temperature increases throughout the ice column on 26 December 2020 at

503   the Level 2 site and on 10 February 2021 at the Level 1 site (Figure 3a and 3b). Such an abrupt rise in ice temperatures can

504   only be explained by an upward infiltration of warm seawater through newly-formed cracks in the ice as a result of these

505   fracturing events. Both dynamic events led to the reduced ice growth rate and associated latent heat flux (Figure 8a and 8b)

506   due to the upward infiltration of warm seawater.

507   On 26 December 2020, a weak low-pressure system brought increased air temperatures and higher wind speeds (Figure

508   10a). At the same time, an abrupt pitch change was recorded by the SIMBA data logger (Figure 10b). Seawater upward

509   infiltration, combined with above-zero air temperatures (Figure 10a), led to a rise in ice surface temperature. This

510   subsequently caused the formation of a slush layer, and snow ice formation (Figure 3b). During this event, the conductive

511   heat flux of the upper ice layer shifted to downward, while the specific heat flux exhibited a sudden increase.

512   The storm event on 10 February 2021 was similar to that on 26 December 2020, but low near-surface air temperatures

513   (Figure 10e), prevented the formation of slush at the ice surface. Thus, no snow-ice layer was observed during or after this

514   event. In addition, the temperature rise at the ice surface was very weak and relatively transient during this event (Figure 3a).

515   The conductive heat flux through the top ice layer remained positive, while that through the lower ice layer was strongly

516   reduced. This implied that the influence of the ice fracturing on the heat flux in the ice interior had not yet reached the ice

517   surface. The sudden increase of specific heat flux was more drastic than that observed in December because the ice layer had

518   been sufficiently cooled before the event in February. This dynamic event presumably also contributed to the buoy failure

519   soon after (by 26 February 2021).

520   The formation of snow ice and superimposed ice not only directly contribute to the ice mass balance but also alter

521   active and passive microwave signals, which in turn affect any satellite remote sensing retrievals of sea ice geophysical

522   variables. Such an effect has already been identified for the rain-on-ice event occurred on 13–14 September 2020 (Gabarró et

523   al., 2022; Stroeve et al., 2022). As we have shown, subsequent close-to-zero air temperature and dynamic deformation events

524   may promote the temporary melting of snow and the formation of snow ice or superimposed ice even during winter. Our

525   study lays the foundation to further look into multi-source satellite remotely-sensed products to clarify the impacts of these

526   events on active and passive microwave signals. The more frequent occurrence of warm and humid air mass intrusions from

527   lower latitudes may significantly increase the cumulative impact of warming events during winter in the central Arctic Ocean

528   (e.g., Graham et al., 2017). Therefore, the impact of the mechanisms described above on the heat balance of the sea ice

529   surface and their effect on microwave signals deserve further attention.

530
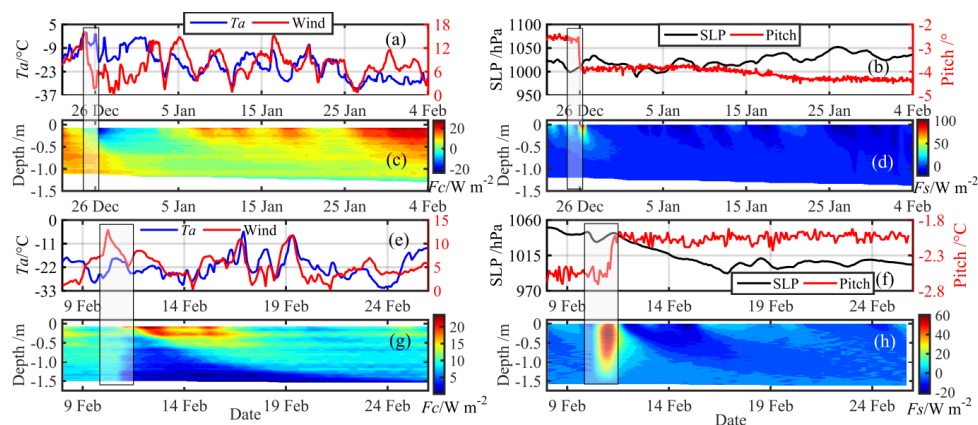
Figure 10. Time series of (a) near-surface air temperature measured at the Level 2 site and wind speed obtained from reanalysis data; (b)

sea level air pressure and pitch of the instrument; (c and d) conductive and specific heat fluxes through the ice cover from 22 December

2020 to 4 February 2021 with a dynamic event on 26 December. (e–h) Same as panels (a–d), but obtained at the Level 1 site from 8 to 21

February 2021 with a dynamic event on 10 February.

4.2 Comparisons with previous observations of sea ice mass balance in the TPD region

Considering the observations at the Level 2 site as representative of the general CO3 ice floe properties, we used these

data for comparison to similar historic SIMBA datasets deployed in the TPD region during the previous 6 years (Figure 1).

Generally, the level ice on the CO3 floe exhibited a moderate sea ice growth rate compared to the observations obtained by

the other 11 buoys. The statistical analysis (Figure S2 in Supplementary material) reveals that both the drifting pattern,

associated with the changes in the CAI, and the equivalent ice thickness, i.e., the ice thickness plus three times the snow

depth (Lei et al., 2022), strongly modulate the sea ice growth. The September–February CAI in the study year was lower

than in the other years under consideration, which resulted in the CO3 floe remaining at comparably high latitudes (86.1°N

by 1 March 2021). However, the rapid southward advection of the floe in March–April 2021 resulted in a mediocre latitude

of 83.3°N (17 April 2021) where the maximum ice thickness and near-average ice growth were observed. The relatively thin

ice thickness (1.16 m) and thick snow depth (0.24 m) at the CO3 floe resulted in the moderate equivalent thickness and onset

of ice basal growth (23 November 2020), as well as the near-average time when maximum ice thickness was observed.

Combining the ice draft data obtained from the upward-looking sonars deployed in the Fram Strait and the drifting pattern of

the floes before reaching the Fram Strait, Sumata et al. (2022) revealed that the longer time with the floes staying in the

region south of 82°N could be related to the greater reduce of ice thickening because of the increased oceanic heat flux there.

Thus, for the MOSAiC CO3 floe, the drifting pattern, of staying at higher latitudes for a long time and crossing rapidly the

region south of 82°N, was actually beneficial for the ice thickening before reaching the Fram Strait.

Thus, the ice growth observed in the study year was the integrated result of multiple contributing factors, including a

553   low southward advection in September–February, a rapid southward advection in the following months, a comparably low

554   initial ice thickness, and the presence of a relatively thick snow cover throughout the ice growth season. The combination of

555   these individual factors determines the overall regulation of the ice growth, i.e. these factors can either (partially) balance

556   each other out, or enhance each other's effects. Consequently, the total ice basal growth of 0.36 m observed at the Level 2

557   site was generally comparable to the average (0.37±0.12 m) obtained from measurements by all available buoys (7 of the 11

558   additional datasets covered the entire ice growth season). Thus, the measurements at the Level 2 site can be considered as a

559   reference for ice growth in the TPD region, and the results derived from this study can provide important validation data for

560   sea ice numerical models. However, our study also suggests that the refreezing of melt ponds, rotten ice, and unconsolidated

561   ridge layers do play an important role in the ice heat budget and mass balance and, if neglected in a numerical simulation, the

562   ice growth rate can be significantly overestimated.

563   **5 Summary and conclusions**

564   In this study, we analyzed data collected by four SIMBA-type ice mass balance buoys during their journey through the

565   Arctic Transpolar Drift in 2020/21. The buoys were deployed on an ice floe close to the geographic North Pole in

566   August-September 2020, as part of the second drift of the year-long MOSAiC experiment. This study aimed to fill

567   knowledge gaps related to the freezing processes of different sea ice types such as melt ponds and unconsolidated ridges.

568   These crucially important processes could not be investigated during the first MOSAiC drift (October 2019 – July 2020), as

569   the original floe (as well as all sites of the wider Distributed Network) broke apart in Fram Strait well before the start of the

570   subsequent freezing season (Nicolaus et al., 2022).

571   We investigated in great detail four sets of temperature profile time series obtained by thermistor chains installed at

572   different sites representative of the general ice conditions at the time: two level ice sites, an initially open melt pond, and a

573   small ridge. Our analysis reveals that several factors together shaped the seasonal evolution of the sea ice mass balance at

574   our measurement sites: 1) the general ice drift pattern, 2) the comparably small initial ice thickness, 3) the large snow

575   accumulation especially on the melt ponds, 4) the relatively warm air temperatures, and 5) the frequent presence of

576   low-pressure systems.

577   The melt pond surface refroze on 5 September 2020. The freezing front reached the bottom of the level ice by the end of

578   October 2022, which marked the start of the basal ice growth. The total ice basal growth for the level ice with an initial

579   thickness of 1.16 m was 0.36 m. The maximum thickness was observed on 17 April 2021. Both the timing and amount of the

580   ice basal growth were comparable with measurements collected by 11 other buoys that drifted along a similar path during the

581   previous 6 years. The refreezing of the meltwater within the pond and the brine channels within the underlying rotten ice

582   layer delayed the cooling of the ice layer and the ice basal growth at the pond site. Even by mid-February 2021, when the

583   pond buoy finally failed, the ice temperature gradient at the pond site was not yet established, and ice basal growth was still

584   not observed.

585   Through a combination of the temperature data obtained on the ridge and nearby level ice, we were able to estimate the

586   macroporosity of the unconsolidated layer within the ridge. Based on the heat balance at the interface between the

587   consolidated and unconsolidated layers, the macroporosity of the unconsolidated layer was estimated between 0.005 and

588   0.755. This macroporosity significantly increases the consolidation rate compared to the level ice growth rate. However,

589   ridge keel basal growth was not observed until the end of April 2021, and thereby lagged significantly behind the level ice.

590   We conclude that increased areal fractions of melt ponds and unconsolidated ridges at the end of the melt season have the

591   potential to significantly reduce the growth rate in winter. The role of melt ponds and unconsolidated ridges in the sea ice

592   mass balance especially at the basin scale needs to be assessed further using numerical models with improved

593   parameterizations.

594   The rain-on-snow event on 13–14 September 2021 resulted in the melt of snow and the subsequent formation of a

595   superimposed ice layer of 0.08 m on top of the refrozen pond. Close-to-zero air temperatures were observed on 25

596   September, 12 November, and 24 December 2020, which were accompanied by subsequent warming of the snow and top ice

597   layer. Especially the event on 25 September 2020 resulted in the formation of superimposed ice on one of the level ice sites.

598   In addition, two ice fracturing events, associated with passing storms, were identified from the data on 26 December 2020

599   and 10 February 2021. Both of these events resulted in an upward infiltration of seawater and sudden warming of the entire

600   ice column. The dynamic event on 26 December 2020, combined with the preceding close-to-zero air temperatures from 24

601   to 26 December 2020, resulted in the formation of a 0.12 m thick snow-ice layer.

602   As the ice floe drifted towards Fram Strait and the Greenland Sea, and especially during the drift close to the ice edge,

603   the oceanic heat flux under the ice increased rapidly, reaching as much as 70 W m^{-2} at 77.5°N by 9 June 2021. As a result,

604   the melt rate at the ice bottom exceeded that at the surface. In the MIZ, the impact of ocean upward mixing on the ice basal

605   melt can be further analyzed in combination with the full dataset measured by the CTD buoy. The knowledge derived from

606   this study can directly support the ongoing studies under the MOSAiC multidisciplinary cooperation and advance

607   interpretation of sea ice thermodynamic process relying on the data obtained from other individual IMB measurements.

608   **Data availability**

609   All the buoy data were initially archived in the online sea-ice knowledge and data platform at www.meereisportal.de and will

610   be available in the PANGAEA online repository before the final publication according to the MOSAiC data policy.

611   Sea ice concentration data was obtained from https://nsidc.org/data/G02202/versions/4 (last access on 6 December 2022).

612   Sea ice thickness was downloaded from merged CryoSat-2 and SMOS (https://data.seaiceportal.de/data/cs2smos_awi/v204/;

613   last access on 6 December 2022). The ERA5 atmospheric reanalysis data were downloaded from

614   https://www.ecmwf.int/en/forecasts/datasets/reanalysis-datasets/era5 (last access on 6 December 2022).

Author contributions

616   Conception, design, and initial manuscript draft: RL.

617   Providing the buoys for deployment: RL, BC, MN, BR, MH.

618   Deployment of the buoys: MH, MN, JR.

619   Processing, analysis and interpreting of data: all authors.

620   Writing or revision and approval of the submitted manuscript: all authors.

Competing interests

622   One of the co-authors is a member of the editorial board of the Cryosphere, and the authors declare that they have no other

623   conflict of interest.

Acknowledgments

625   Data used in this manuscript was produced as part of the international Multidisciplinary drifting Observatory for the Study of

626   the Arctic Climate (MOSAiC) with the tag MOSAiC20192020 (AWI_PS122_5) and the Chinese program for MOSAiC

627   funded by the CAA. We thank the crew of the R/V *Polarstern* for their great logistical support during the deployment of the

628   buoys. We thank all those who contributed to MOSAiC and made this endeavor possible (Nixdorf et al., 2021).

Financial support

630   This work was supported by grants from the National Natural Science Foundation of China (41976219, 42106231 and

631   41722605), the National Key Research and Development Program (2021YFC2803304), the German Federal Ministry of

632   Education and Research (BMBF) through financing the Alfred Wegener Institute, Helmholtz Centre for Polar and Marine

633   Research (AWI) and the *Polarstern* expedition PS122 under the grant N-2014-H-060_Dethloff, and the AWI through its

634   projects: AWI_ROV, AWI_ICE, AWI_SNOW. The AWI buoy program was partly funded by the Helmholtz strategic

635   investment Frontiers in Arctic Marine Monitoring (FRAM). BC was supported by the Academy of Finland under contract

636   317999. MH, MN, JR, and BR were supported by AWI internal funds. DP was supported by US National Science

637   Foundation Office of Polar Programs 1724424 and 1724540.

References

639   Anhaus, P., Katlein, C., Nicolaus, M., Hoppmann, M., and Haas, C.: From bright windows to dark spots: Snow cover
640   controls melt pond optical properties during refreezing. Geophysical Research Letters, 48, e2021GL095369. https://doi.
641   org/10.1029/2021GL095369, 2021.

642   Cox, G.F.N., and Weeks, W.F.: Equations for determining the gas and brine volumes in sea-ice samples, J. Glaciol., 29(102),
643   306–316, doi:10.3189/S0022143000008364, 1983.

644   Chai, W., Leira, B.J., Naess, A., Høyland, K.V., and Ehlers, S.: Development of environmental contours for first-year ice
645   ridge statistics, Struct. Saf., 87, doi:10.1016/j.strusafe.2020.101996, 2020.

646   Duarte, P., Sundfjord, A., Meyer, A., Hudson, S. R., Spreen, G., and Smedsrud, L. H.: Warm Atlantic water explains
647   observed sea ice melt rates north of Svalbard, J. Geophys. Res. Oceans., 125,
648   e2019JC015662. https://doi.org/10.1029/2019JC015662, 2020.

649   Ervik, A., Hoyland, K., Shestov, A., and Nord, T. S.: On the decay of first-year ice ridges: measurements and evolution of
650   rubble macroporosity, ridge drilling resistance and consolidated layer strength, Cold. Reg. Sci. Technol., 151, 196–207,
651   doi:10.1016/j.coldregions.2018.03.024, 2018.

652   Farrell, S. L., Duncan, K., Buckley, E. M., Richter-Menge, J., and Li, R.: Mapping sea ice surface topography in high fidelity
653   with ICESat-2, Geophys. Res. Lett., 47, e2020GL090708, doi:10.1029/2020GL090708, 2020.

654   Fernández-Méndez, M., Olsen, L. M., Kauko, H. M., Meyer A., Rösel A., Merkouriadi, I., Mundy, C. J., Ehn, J. K.,
655   Johansson, A. M., Wagner, P. M., Ervik, Å., Sorrell B. K., Duarte, P., Wold, A., Hop, H., and Assmy, P.: Algal hot spots
656   in a changing Arctic Ocean: Sea-ice ridges and the snow-ice interface, Front. Marine Sci., 5, doi:
657   10.3389/fmars.2018.00075, 2018.

658   Fetterer, F., Knowles, K., Meier, W. N., Savoie, M., and Windnagel, A. K.: Sea ice index, version 3. Boulder, CO: National
659   Snow and Ice Data Center, doi: 10.7265/N5K072F8, 2017.

660   Gabarró, C., Fabregat, P., Hernández-Macià, F., Jove, R., Salvador, J., Spreen, G., Thielke, L., Dadic, R., Huntemann, M.,
661   Kolabutin, N., Nomura, D., Hannula, H.-R., and Schneebeli, M.: First results of the ARIEL L-band radiometer on the
662   MOSAiC Arctic Expedition during the late summer and autumn period, Elementa-Sci Anthrop., 10(1),
663   doi:10.1525/elementa.2022.00031, 2022.

664   Graham, R. M., Cohen, L., Petty, Boisvert,   A. A.,L. N., Rinke, A., Hudson, S. R,Nicolaus, M., and Granskog, M. A.:
665   Increasing frequency and duration of Arctic winter warming events, Geophys. Res. Lett., 44,
666   doi:10.1002/2017GL073395, 2017.

667   Hancke, K., Kristiansen, S., and Lund-Hansen, L.: Highly productive ice algal mats in Arctic melt ponds: primary production
668   and carbon turnover, Front. Marine Sci., 9, doi: 10.3389/fmars.2022.841720, 2022.

669   Hansen, E., Ekeberg, O. C., Gerland, S., Pavlova, O., Spreen, G., and Tschudi, M.: Variability in categories of Arctic sea ice

670   in Fram Strait, J. Geophys. Res. Oceans., 119, 7175–7189, doi:10.1002/2014JC010048, 2014.

671   Høyland, K.V.: Consolidation of first-year sea ice ridges, J. Geophys. Res. Oceans., 107(C6),
672   doi:10.1029/2000JC000526, 2002.

673   Høyland, K.V., and Løset, S.: Measurements of temperature distribution, consolidation and morphology of a first-year sea ice
674   ridge, Cold. Reg. Sci. Technol., 29(1), 59–74, doi:10.1016/S0165-232X(99)00004-X, 1999.

675   Hoppmann, M., Karam, S., Allerholt, J., Koenig, Z., Kuznetsov I., Fang Y., Rabe B.,: Unprocessed seawater temperature,
676   conductivity and salinity obtained by CTD buoy 2020O10 deployed on MOSAiC Leg 5
677   (PS122/5). PANGAEA, https://doi.pangaea.de/10.1594/PANGAEA.955343, 2023.

678   Jackson, K., Wilkinson, J., Maksym, T., Meldrum, D., Beckers, J., Haas, C., and Mackenzie, D.: A novel and low-cost sea ice
679   mass balance buoy, J. Atmos. Ocean. Tech., 30, 2676–2688, doi:10.1175/jtechd-13-00058.1, 2013.

680   Jakobsson, M., M., Mayer, L., Coakley, B., Dowdeswell, J. A., Forbes, S., Fridman, B., Hodnesdal, H., Noormets, R.,
681   Pedersen, R., Rebesco, M., Schenke, H.W., Zarayskaya, Y., Accettella, D., Armstrong, A., Anderson, R. M., Bienhoff, P.,
682   Camerlenghi, A., Church, I., Edwards, M., Gardner, J. V., Hall, J. K., Hell, B., Hestvik, O., Kristoffersen, Y., Marcussen,
683   C., Mohammad, R., Mosher, D., Nghiem, S. V., Pedrosa, M. T., Travaglini, P. G., and Weatherall, P.: The International
684   Bathymetric Chart of the Arctic Ocean (IBCAO) Version3.0, Geophys. Res. Lett., 39, L12609,
685   doi:10.1029/2012GL052219, 2012.

686   Katlein, C., Mohrholz, V., Sheikin, I., Itkin, P., Divine, D.V., Stroeve, J., Jutila, A., Krampe, D., Shimanchuk, E., Raphael, I.,
687   Rabe, B., Kuznetov, I., Mallet, M., Liu, H., Hoppmann, M., Dumitrascu, A., Arndt, S., Anhaus, P., Nicolaus, M., Matero,
688   I., Oggier, M., Eicken, H., Haas, C.: Platelet ice under Arctic pack ice in winter, Geophysical Research Letters 47(16),
689   doi: http://dx.doi.org/10.1029/2020gl088898, 2020.

690   Katlein, C., Langelier, J.-P., Ouellet, A., Lévesque-Desrosiers, F., Hisette, Q., Lange, B. A., Lambert-Girard, S., Babin, M.,
691   Thibault, S.: The Three-Dimensional Light Field Within Sea Ice Ridges, Geophys. Res. Lett., 48(11), e2021GL093207,
692   doi: 10.1029/2021GL093207, 2021.

693   Kawaguchi, Y., Koenig, Z., Nomura, D., Hoppmann, M., Inoue, J., Fang, Y., Schulz, K., Gallagher M., Katlein C., Nicolaus
694   M., and Rabe B.: Turbulent mixing during late summer in the ice–ocean boundary layer in the central Arctic Ocean:
695   Results from the MOSAiC expedition, J. Geophys. Res. Oceans., 127, e2021JC017975, doi:10.1029/2021JC017975,
696   2022.

697   Kharitonov, V. V.: Internal structure and porosity of ice ridges investigated at North Pole-38 drifting station, Cold. Reg. Sci.
698   Technol., 82, 144–152, doi: 10.1016/j.coldregions.2012.05.018, 2012.

699   Kim, J. H., Moon, W., Wells, A. J., Wilkinson, J. P., Langton, T., Hwang, B., Granskog, M. A., and Rees Jones, D. W.:
700   Salinity control of thermal evolution of late summer melt ponds on Arctic sea ice, Geophysical Research Letters, 45,
701   8304–8313, https://doi.org/10.1029/2018GL078077, 2018.

702   Krumpen, T., Birrien, F., Kauker, F., Rackow, T., von Albedyll, L., Angelopoulos, M., Belter, H.J., Bessonov, V., Damm, E.,
703   Dethloff, K., Haapala, J., Haas, C., Harris, C., Hendricks, S., Hoelemann, J., Hoppmann, M., Kaleschke, L., Karcher,
704   M., Kolabutin, N., Lei, R., Lenz, J., Morgenstern, A., Nicolaus, M., Nixdorf, U., Petrovsky, T., Rabe, B., Rabenstein, L.,
705   Rex, M., Ricker, R., Rohde, J., Shimanchuk, E., Singha, S., Smolyanitsky, V., Sokolov, V., Stanton, T., Timofeeva, A.,
706   Tsamados, M., and Watkins, D.: The MOSAiC ice floe: sediment-laden survivor from the Siberian shelf, The
707   Cryosphere, 14, 2173–2187, doi:10.5194/tc-14-2173-2020, 2020.

708 Lambert-Girard, S., Babin, M., and Thibault, S.: The three-dimensional light field within sea ice ridges, Geophys. Res. Lett.,
709   48, e2021GL093207, doi:10.1029/2021GL093207, 2021.

710 Landy, J. C., Dawson, G. J., Tsamados, M., Bushuk, M., Stroeve, J., Howell, S., Krumpen, T., Babb, D. Komarov, A.,
711   Heorton, H., Belter, H. J., and Aksenov, Y.: A year-round satellite sea-ice thickness record from CryoSat-2, Nature, 609,
712   517–522, doi:10.1038/s41586-022-05058-5, 2022.

713 Lee, S., Stroeve, J., Tsamados, M., and Khan A. L.: Machine learning approaches to retrieve pan-Arctic melt ponds from
714   visible satellite imagery, Remote. Sens. Environ., 247, 111919, doi:10.1016/j.rse.2020.111919, 2020.

715 Lei, R., Gui, D., Hutchings, J.K., Heil, P. and Li, N.: Annual cycles of sea ice motion and deformation derived from buoy
716   measurements in the Western Arctic Ocean over two ice seasons, J. Geophys. Res. Oceans., 125(6), e2019JC015310,
717   doi:10.1029/2019jc015310, 2020.

718 Lei, R., Cheng, B., Hoppmann, M., Zhang, F., Zuo, G., Hutchings, J. K., Lin, L., Lan, M., Wang, H., Regnery, J., Krumpen,
719   T., Haapala, J., Rabe, B., Perovich, D. K., and Nicolaus, M.: Seasonality and timing of sea ice mass balance and heat
720   fluxes in the Arctic transpolar drift during 2019–2020, Elementa-Sci Anthrop., 10 (1), doi:
721   10.1525/.elementa.2021.000089, 2022.

722 Leppäranta, M.: A review of analytical sea ice growth models, Atmos. Ocean., 31(1), 123–138, doi:10.1080/070559
723   00.1993.9649465,1993.

724 Leppäranta, M., Lensu, M., Kosloff, P. and Veitch, B.: The life story of a first-year sea ice ridge, Cold. Reg. Sci. Technol.,
725   23(3), 279–290, doi: 10.1016/0165-232X(94)00019-T, 1995.

726 Light, B., Smith, M. M., Perovich, D. K., Webster, M. A., Holland, M. M., Linhardt, F., Raphael, I. A., ClemensS
727   ewall, D., Macfarlane, A. R., Anhaus, P., and Bailey, D.A.: Arctic sea ice albedo: Spectral composition, spatial
728   heterogeneity, and temporal evolution observed during the MOSAiC drift, Elementa-Sci Anthrop., 10(1), doi:1
729   0.1525/elementa.2021.000103, 2022.

730 Lin, L., Lei, R., Hoppmann, M., Perovich, D. K., and He, H.: Changes in the annual sea ice freeze–thaw cycle in the Arctic
731   Ocean from 2001 to 2018, The Cryosphere, 16, 4779–4796, doi:10.5194/tc-16-4779-2022, 2022.

732 Lu, P., Cao, X., Wang, Q., Leppäranta, M.,Cheng, B., and Li, Z.: Impact of a surface ice lid on the optical properties of melt
733   ponds, J. Geophys. Res. Oceans.,123, 313–8328, doi:10.1029/2018JC014161, 2018.

734 McPhee, M.G., and Untersteiner, N.: Using sea ice to measure vertical heat flux in the ocean, J. Geophys. Res. Oceans.,
735   87(C3), 2071–2074, doi:10.1029/JC087iC03p02071, 1982.

736 Nicolaus, M., Perovich, D. K., Spreen, G., Granskog, M. A., von Albedyll, L., Angelopoulos, M., Anhaus, P., Arndt, S.,
737   Belter, H. J., Bessonov, V., Birnbaum, G., Brauchle, J., Calmer, R., Cardellach, E., Cheng, B., Clemens-Sewall, D.,
738   Dadic, R., Damm, E., de Boer, G., Demir, O., Dethloff, K., Divine, D. V., Fong, A. A., Fons, S., Frey, M. M., Fuchs, N.,
739   Gabarró, C., Gerland, S., Goessling, H. F., Gradinger, R., Haapala, J., Haas, C., Hamilton, J., Hannula, H.-R., Hendricks,
740   S., Herber, A., Heuzé, C., Hoppmann, M., Høyland, K. V., Huntemann, M., Hutchings, J. K., Hwang, B., Itkin, P.,
741   Jacobi, H.-W., Jaggi, M., Jutila, A., Kaleschke, L., Katlein, C., Kolabutin, N., Krampe, D., Kristensen, S. S., Krumpen,
742   T., Kurtz, N., Lampert, A., Lange, B. A., Lei, R., Light, B., Linhardt, F., Liston, G. E., Loose, B., Macfarlane, A. R.,
743   Mahmud, M., Matero, I. O., Maus, S., Morgenstern, A., Naderpour, R., Nandan, V., Niubom, A., Oggier, M., Oppelt, N.,
744   Pätzold, F., Perron, C., Petrovsky, T., Pirazzini, R., Polashenski, C., Rabe, B., Raphael, I. A., Regnery, J., Rex, M.,
745   Ricker, R., Riemann-Campe, K., Rinke, A., Rohde, J., Salganik, E., Scharien, R. K., Schiller, M., Schneebeli, M.,

746   Semmling, M., Shimanchuk, E., Shupe, M. D., Smith, M. M., Smolyanitsky, V., Sokolov, V., Stanton, T., Stroeve, J.,
747   Thielke, L., Timofeeva, A., Tonboe, R. T., Tavri, A., Tsamados, M., et al.: Overview of the MOSAiC expedition: Snow
748   and sea ice, Elementa-Sci Anthrop., 10, 000046, doi:10.1525/elementa.2021.000046, 2022.

749   Nicolaus, M., Katlein, C., Maslanik, J., and Hendricks, S.: Changes in Arctic sea ice result in increasing light transmittance
750   and absorption, Geophys. Res. Lett. 39(24), L24501. doi: 10.1029/2012GL053738, 2012.

751   Nixdorf, U., Dethloff, K., Rex, M., Shupe, M., Sommerfeld, A., Perovich, D. K., Nicolaus, M., Heuzé, C., Rabe, B., Loose,
752   B., Damm, E., Gradinger, R., Fong, A., Maslowski, W., Rinke, A., Kwok, R., Spreen, G., Wendisch, M., Herber, A.,
753   Hirsekorn, M., Mohaupt, V., Frickenhaus, S., Immerz, A., WeissTuider, K., König, B., Mengedoht, D., Regnery, J.,
754   Gerchow, P., Ransby, D., Krumpen, T., Morgenstern, A., and Haas, C.: MOSAiC extended acknowledgement, Zenodo,
755   doi:10.5281/zenodo.5179738, 2021.

756   Nixdorf, U., Dethloff, K., Rex, M., Shupe, M., Sommerfeld, A., Perovich, D. K., Nicolaus, M., Heuzé, C., Rabe, B., Loose,
757   B., Damm, E., Gradinger, R., Fong, A., Maslowski, W., Rinke, A., Kwok, R., Spreen, G., Wendisch, M., Herber, A.,
758   Hirsekorn, M., Mohaupt, V., Frickenhaus, S., Immerz, A., Weiss-Tuider, K., König, B., Mengedoht, D., Regnery, J.,
759   Gerchow, P., Ransby, D., Krumpen, T., Morgenstern, A., Haas, C., Kanzow, T., Rack, F. R., Saitzev, V., Sokolov, V.,
760   Makarov, A., Schwarze, S., Wunderlich, T., Wurr, K., and Boetius, A.: MOSAiC Extended Acknowledgement, Zenodo,
761   doi:10.5281/zenodo.5541624, 2021.

762   Perovich, D.K., Grenfell, T.C., Light, B., and Hobbs, P.V.: Seasonal evolution of the albedo of multiyear Arctic Sea ice, J.
763   Geophys. Res. Oceans., 107, 20–13, doi: 10.1029/2000JC000438, 2002.

764   Perovich, D. K., and Elder, B.: Estimates of ocean heat flux at SHEBA, Geophys. Res. Lett., 29(9), 1344,
765   doi:10.1029/2001GL014171, 2002.

766   Persson, P. O. G.: Onset and end of the summer melt season over sea ice: thermal structure and surface energy perspective
767   from SHEBA, Clim. Dyn., 39, 1349–1371, doi:10.1007/s00382-011-1196-9, 2012.

768   Provost, C., Sennéchael, N., and Sirven, J.: Contrasted summer processes in the sea ice for two neighboring floes north of
769   84°N: Surface and basal melt and false bottom formation, J. Geophys. Res. Oceans., 124, 3963–3986,
770   doi:10.1029/2019JC015000, 2019.

771   Rabe, B., Heuzé, C., Regnery, J., Aksenov, Y., Allerholt, J., Athanase, M., Bai, Y., Basque, C., Bauch, D., Baumann, T.M.,
772   Chen, D., Cole, S.T., Craw, L., Davies, A., Damm, E., Dethloff, K., Divine, D.V., Doglioni, F., Ebert, F., Fang,Y., Fer, I.,
773   Fong, A.A., Gradinger, R., Granskog, M.A., Graupner, R., Haas, C., He, H., He, Y., Hoppmann, M., Janout, M., Kadko,
774   D., Kanzow, T., Karam, S., Kawaguchi, Y., Koenig, Z., Kong, B., Krishfield, R.A., Krumpen, T., Kuhlmey, D.,
775   Kuznetsov, I., Lan, M., Laukert, G., Lei, R., Li, T., TorresValdés, S., Lin, L., Lin, L., Liu, H., Liu, N., Loose, B., Ma, X.,
776   MacKay, R., Mallet, M., Mallett, R.D.C., Maslowski, W., Mertens, C., Mohrholz, V., Muilwijk, M., Nicolaus, M.,
777   O'Brien, K., Perovich, D., Ren, J., Rex, M., Ribeiro, N., Rinke, A., Schaffer, J., Schuffenhauer, I., Schulz, K., Shupe,
778   M.D., Shaw, W., Sokolov, V., Sommerfeld, A., Spreen, G., Stanton, T., Stephens, M., Su, J., Sukhikh, N., Sundfjord, A.,
779   Thomisch, K., Tippenhauer, S., Toole, J.M., Vredenborg, M., Walter, M., Wang, H., Wang, L., Wang, Y., Wendisch, M.,
780   Zhao, J., Zhou, M., Zhu, J.: Overview of the MOSAiC expedition: Physical oceanography. Elementa: Science of the
781   Anthropocene 10(1). doi: https://doi.org/10.1525/elementa.2021.00062, 2022.

782   Rampal, P., Weiss, J. and Marsan, D.: Positive trend in the mean speed and deformation rate of Arctic sea ice, 1979–2007, J.
783   Geophys. Res., 114(C5), C05013, doi:10.1029/2008jc005066, 2009.

784   Ricker, R., Hendricks, S., Helm, V., Skourup, H., and Davidson, M.: Sensitivity of CryoSat-2 Arctic sea-ice freeboard and

785   thickness on radar-waveform interpretation, The Cryosphere, 8, 1607–1622, doi:10.5194/tc-8-1607-2014, 2014.

786   Ricker, R., Hendricks, S., Kaleschke, L., Tian-Kunze, X., King, J., and Haas, C.: A weekly Arctic sea-ice thickness data
787   record from merged CryoSat-2 and SMOS satellite data, The Cryosphere, 11(4), 1607–1623,
788   doi:10.5194/tc11-1607-2017, 2017.

789   Rinke, A., Cassano, J.J., Cassano, E.N., Jaiser, R., and Handorf, D.: Meteorological conditions during the MOSAiC
790   expedition: Normal or anomalous? Elementa-Sci Anthrop., 9(1), doi:10.1525/elementa.2021.00023, 2021.

791   Shafrova, S., and Høyland, K. V.: Morphology and 2D spatial strength distribution in two Arctic first-year sea ice ridges,
792   Cold. Reg. Sci. Technol., 51, 38–55, doi: 10.1016/j.coldregions.2007.05.011, 2008.

793   Schroder, D., Feltham, D.L., Flocco, D., and Tsamados, M.: September Arctic sea ice minimum predicted by spring
794   melt-pond fraction, Nat. Clim. Chang, 4, 353–357, doi:10.1038/NCLIMATE2203, 2014.

795   Shestov, A., Hoyland, K., and Ervik, A.: Decay phase thermodynamics of ice ridges in the arctic ocean, Cold. Reg. Sci.
796   Technol., 152, 23–34, doi:10.1016/j.coldregions.2018.04.005, 2018.

797   Shupe, M.D., Rex, M., Blomquist, B., Persson, P.O.G., Schmale, J., Uttal, T., Althausen, D., Angot, H., Archer, S., Bariteau,
798   L., Beck, I., Bilberry, J., Bucci, S., Buck, C., Boyer, M., Brasseur, Z., Brooks, I.M., Calmer, R., Cassano, J., Castro, V.,
799   Chu, D., Costa, D., Cox, C.J., Creamean, J., Crewell, S., Dahlke, S., Damm, E., de Boer, G., Deckelmann, H, Dethloff,
800   K, Dütsch, M, Ebell, K, Ehrlich, A, Ellis, J, Engelmann, R, Fong, AA, Frey, MM, Gallagher, MR, Ganzeveld, L.,
801   Gradinger, R., Graeser, J., Greenamyer, V., Griesche, H., Griffiths, S., Hamilton, J., Heinemann, G., Helmig, D., Herber,
802   A., Heuzé, C., Hofer, J., Houchens, T., Howard, D., Inoue, J., Jacobi, H.-W., Jaiser, R., Jokinen, T., Jourdan, O., Jozef,
803   G., King, W., Kirchgaessner, A., Klingebiel, M., Krassovski, M., Krumpen, T., Lampert, A., Landing, W., Laurila, T.,
804   Lawrence, D., Lonardi, M., Loose, B., Lüpkes, C., Maahn, M., Macke, A., Maslowski, W., Marsay, C., Maturilli, M.,
805   Mech, M., Morris, S., Moser, M., Nicolaus, M., Ortega, P., Osborn, J., Pätzold, F., Perovich, D.K., Petäjä, T,. Pilz, C.,
806   Pirazzini, R., Posman, K., Powers, H., Pratt, K.A., Preußer, A., Quéléver, L., Radenz, M., Rabe, B., Rinke, A., Sachs, T.,
807   Schulz, A., Siebert, H., Silva, T., Solomon, A., Sommerfeld, A., Spreen, G., Stephens, M., Stohl, A., Svensson, G., Uin,
808   J., Viegas, J., Voigt, C., von der Gathen, P., Wehner, B., Welker, J.M., Wendisch, M., Werner, M., Xie, Z., Yue, F.:
809   Overview of the MOSAiC expedition: Atmosphere. Elementa: Science of the Anthropocene, 10(1). doi:
810   https://doi.org/10.1525/elementa.2021.00060. 2022.

811   Stroeve, J., and Notz, D.: Changing state of Arctic sea ice across all seasons, Environ. Res. Lett., 13, 10.
812   doi: 10.1088/1748-9326/aade56, 2018.

813   Stroeve, J., Nandan, V., Willatt, R., Dadic, R., Rostosky, P., Gallagher, M., Mallett, R., Barrett, A., Hendricks, S., Tonboe, R.,
814   McCrystall, M., Serreze, M., Thielke, L., Spreen, G., Newman, T., Yackel, J., Ricker, R., Tsamados, M., Macfarlane, A.,
815   Hannula, H.-R., and Schneebeli M.: Rain on snow (ROS) understudied in sea ice remote sensing: a multi-sensor
816   analysis of ROS during MOSAiC (Multidisciplinary drifting Observatory for the Study of Arctic Climate), The
817   Cryosphere, 16, 4223–4250, doi:10.5194/tc-16-4223-2022, 2022.

818   Strub-Klein, L., and Sudom, D.: A comprehensive analysis of the morphology of first-year sea ice ridges, Cold. Reg. Sci.
819   Technol., 82, 94–109, doi:10.1016/j.coldregions.2012.05.014, 2012.

820   Sturm, M., Holmgren, J., König, M., and Morris, K.: The thermal conductivity of seasonal snow, J. Glaciol., 43, 26–41,
821   doi:10.3189/S0022143000002781, 1997.

822   Sturm, M., Perovich, D. K., and Holmgren, J.: Thermal conductivity and heat transfer through the snow on the ice of the

823   Beaufort Sea, J. Geophys. Res., 107(C10), 8043, doi:10.1029/2000JC000409, 2002.

824   Sumata, H., de Steur, L., Gerland, S., Divine, D. V., and Pavlova, O.: Unprecedented decline of Arctic sea ice outflow in

825   2018. Nature Communications, 13, 1747, https://doi.org/10.1038/s41467-022-29470-7, 2022.

826   Tschudi, M.A., Meier, W.N., and Stewart, J.S.: An enhancement to sea ice motion and age products at the National Snow and

827   Ice Data Center (NSIDC), The Cryosphere, 14, 1519–1536, doi:10.5194/tc-14-1519-2020, 2020.

828   Vihma, T., Tisler, P., and Uotila, P.: Atmospheric forcing on the drift of Arctic sea ice in 1989–2009, Geophys. Res. Lett., 39,

829   doi: 10.1029/2011GL050118, 2012.

830   von Albedyll, L., Hendricks, S., Grodofzig, R., Krumpen, T., Arndt, S., Belter, H.J., Cheng, B., Birnbaum, G., Hoppmann,

831   M., Hutchings, J., Itkin, P., Lei, R., Nicolaus, M., Ricker, R., Rohde, J., Suhrhoff, M., Timofeeva, A., Watkins, D.,

832   Webster, M., and Haas, C.: Thermodynamic and dynamic contributions to seasonal Arctic sea ice thickness distributions

833   from airborne observations, Elementa-Sci Anthrop., 10 (1), doi:10. 1525/elementa.2021.00074, 2022.

834   Wagner, D. N., Shupe, M. D., Cox, C., Persson, O. G., Uttal, T., Frey, M. M., Kirchgaessner, A., Schneebeli, M., Jaggi, M.,

835   Macfarlane, A. R., Itkin, P., Arndt, S., Hendricks, S., Krampe D., Nicolaus, M., Ricker, R., Regnery, J., Kolabutin, N.,

836   Shimanshuck, E., Oggier, M., Raphael, I., Stroeve, J., and Lehning, Michael.: Snowfall and snow accumulation during

837   the MOSAiC winter and spring seasons, The Cryosphere, 16, 2373–2402, doi:10.5194/tc-16-2373-2022, 2022.

838   Weeks, W.F.: On Sea Ice. University of Alaska Press. Fairbanks, Alaska. ISBN 978-1-60223-079-8. 664p, 2010.

839   Webster, M. A., Holland, M., Wright, N.C., Hendricks, S., Hutter, N., Itkin, P., Light, B., Linhardt, F., Perovich, D. K.,

840   Raphael, I.A., Smith, M. M., von Albedyll, L., and Zhang, J.: Spatiotemporal evolution of melt ponds on Arctic seaice:

841   MOSAiC observations and model results, Elementa-Sci Anthrop., 10(1), doi:10.1525/elementa.2021.000072, 2022.

842   Wettlaufer, J.: Heat flux at the ice-ocean interface, J. Geophys. Res. Oceans., 96, 7215–7236, doi:10.1029/90JC00081, 1991.

843   Zhang, F., Pang, X., Lei, R., Zhai, M., Zhao, X., and Cai, Q.: Arctic sea ice motion change and response to atmospheric

844   forcing between 1979 and 2019, Int. J. Climatol., 42(3), 1854-1876, doi:10.1002/joc.7340, 2021.

845